

FINAL REPORT

AOARD-04-4026

**“InGaN/GaN Quantum Dots --- Growth, Nano-structure Material
Analysis, and Optical Characterization”**

Chih-Chung (C. C.) Yang

**Graduate Institute of Electro-Optical Engineering
National Taiwan University,**

No. 1 Roosevelt Road, Section 4, Taipei, Taiwan

(phone) 886-2-23657624 (fax) 886-2-23652637 (e-mail) ccy@cc.ee.ntu.edu.tw

April 27, 2005

Report Documentation Page				Form Approved OMB No. 0704-0188	
Public reporting burden for the collection of information is estimated to average 1 hour per response, including the time for reviewing instructions, searching existing data sources, gathering and maintaining the data needed, and completing and reviewing the collection of information. Send comments regarding this burden estimate or any other aspect of this collection of information, including suggestions for reducing this burden, to Washington Headquarters Services, Directorate for Information Operations and Reports, 1215 Jefferson Davis Highway, Suite 1204, Arlington VA 22202-4302. Respondents should be aware that notwithstanding any other provision of law, no person shall be subject to a penalty for failing to comply with a collection of information if it does not display a currently valid OMB control number.					
1. REPORT DATE 19 MAY 2005		2. REPORT TYPE FInal		3. DATES COVERED 27-04-2004 to 27-07-2005	
4. TITLE AND SUBTITLE InGaN/GaN Quantum Dots --- Growth, Nano-structure Material Analysis, and Optical Characterization				5a. CONTRACT NUMBER FA520904P0307	
				5b. GRANT NUMBER	
				5c. PROGRAM ELEMENT NUMBER	
6. AUTHOR(S) Chih-Chung Yang				5d. PROJECT NUMBER	
				5e. TASK NUMBER	
				5f. WORK UNIT NUMBER	
7. PERFORMING ORGANIZATION NAME(S) AND ADDRESS(ES) National Taiwan University, No. 1, Section 4, Roosevelt Road, Taipei 106, Taiwan, TW, 106				8. PERFORMING ORGANIZATION REPORT NUMBER N/A	
9. SPONSORING/MONITORING AGENCY NAME(S) AND ADDRESS(ES) AOARD, UNIT 45002, APO, AP, 96337-5002				10. SPONSOR/MONITOR'S ACRONYM(S) AOARD-044026	
				11. SPONSOR/MONITOR'S REPORT NUMBER(S)	
12. DISTRIBUTION/AVAILABILITY STATEMENT Approved for public release; distribution unlimited					
13. SUPPLEMENTARY NOTES					
14. ABSTRACT we compare the result of strain state analysis (SSA) and photoluminescence (PL) of six InGaN/GaN quantum well samples with un-doped, well-doped, and barrier-doped structures. Based on SSA images, a strain relaxation model is proposed for describing the nanostructure differences between the three sets of sample of different doping conditions. In the barrier-doped samples, the hetero-structure-induced. Therefore, strongly clustering nanostructures (quantum dots) are observed. In the well-doped samples, strain are partially relaxed and the spinodal decompositions are observed. Then, in the Un-doped samples, the un-relaxed strains result in higher miscibility between InN and GaN, Leading to the relatively more uniform composition distributions. Between the Low- and high- indium samples, higher indium content leads to a stronger clustering behavior. The strain relaxations in the well-doped and barrier-doped samples result in their unclear S-Shape behaviors of PL spectral peaks. The enhanced carrier localization and reduced quantum-confined stark effect in the barrier-doped samples are responsible for their significant increases of radiative efficiency.					
15. SUBJECT TERMS Nano-Technology, Photonics, Quantum Dots					
16. SECURITY CLASSIFICATION OF:			17. LIMITATION OF ABSTRACT Same as Report (SAR)	18. NUMBER OF PAGES 42	19a. NAME OF RESPONSIBLE PERSON
a. REPORT unclassified	b. ABSTRACT unclassified	c. THIS PAGE unclassified			

Journal Publications with AFOSR/AOARD Acknowledgements

1. Yung-Chen Cheng, Cheng-Ming Wu, C. C. Yang, Gang Alan Li, Andreas Rosenauer, Kung-Jen Ma, Shih-Chen Shi, and L. C. Chen, "Effects of Interfacial Layers in InGaN/GaN Quantum Well Structures on Their Optical and Nanostructure Properties," accepted for publication in J. Applied Physics. (SCI)
2. Meng-Ku Chen, Yung-Chen Cheng, Jiun-Yang Chen, Cheng-Ming Wu, C. C. Yang, Kung-Jen Ma, Jer-Ren Yang, Andreas Rosenauer, Effects of Silicon Doping on the Nanostructures of InGaN/GaN Quantum Wells," accepted for publication in J. Crystal Growth. (SCI)
3. Hsiang-Chen Wang, Yen-Cheng Lu, Chih-Chung Teng, Yung-Sheng Chen, C. C. Yang, Kung-Jen Ma, Chang-Chi Pan and Jen-Inn Chyi, "Ultrafast Carrier Dynamics in an InGaN Thin Film," J. Applied Physics, Vol. 97, No. 3, pp. 033704-1-4, 2005. (SCI) Also, it was selected for the 2005 issue of Virtual Journal of Ultrafast Science (American Physical Society and the American Institute of Physics).
4. Hsiang-Chen Wang, Shih-Jiun Lin, Yen-Cheng Lu, Yung-Chen Cheng, C. C. Yang, and Kung-Jen Ma, "Carrier Relaxation in InGaN/GaN Quantum Wells with nm-scale Cluster Structures", Applied Physics Letters, Vol. 85, No. 8, pp. 1371-1373, 2004. (SCI)

Abstract

We compare the results of strain state analysis (SSA) and photoluminescence (PL) of six InGaN/GaN quantum well samples with un-doped, well-doped, and barrier-doped structures. Based on the SSA images, a strain relaxation model is proposed for describing the nanostructure differences between the three sets of sample of different doping conditions. In the barrier-doped samples, the hetero-structure-induced strains are fully relaxed such that spinodal decomposition is effectively induced. Therefore, strongly clustering nanostructures (quantum dots) are observed. In the well-doped samples, strains are partially relaxed and the spinodal decomposition process can be slightly induced. Hence, weaker composition fluctuations are observed. Then, in the un-doped samples, the un-relaxed strains result in higher miscibility between InN and GaN, leading to the relatively more uniform composition distributions. Between the low- and high-indium samples, higher indium content leads to a stronger clustering behavior. The strain relaxations in the well-doped and barrier-doped samples result in their unclear S-shape behaviors of PL spectral peaks. The enhanced carrier localization and reduced quantum-confined Stark effect in the barrier-doped samples are responsible for their significant increases of radiative efficiency.

I. Introduction

It has been shown that different doping conditions, including different doping layers, in InGaN/GaN quantum-well (QW) structures led to different optical characteristics. Such effects of silicon doping have been widely studied. Several models were proposed for interpreting the optical and material characteristics of InGaN/GaN QWs with silicon doping. The most commonly used model is the carrier screening effect of the strain-induced piezoelectric field and hence the reduction of the quantum-confined Stark effect (QCSE). This effect leads to the reduced Stokes shift [1-3], the decrease of radiative recombination lifetime [2-4,10], the blue shift of PL spectrum [3,5], and the enhancement of photon emission efficiency [1,3,6]. Also, material analyses have led to the conclusions of growth mode change [6], nanostructure alteration [7], formation of abrupt QW interfaces [2,8], strain relaxation [7,9], and higher potential uniformity in QWs [3]. Meanwhile, it has been shown that different barrier-doping concentrations in InGaN/GaN QW structures resulted in different optical characteristics [11]. These results are not necessarily mutually consistent, particularly in the material nanostructures of such silicon-doped QW samples.

In particular, due to the large lattice mismatch between InN and GaN, indium-rich clusters are usually formed in such a QW structure through spinodal decomposition and other effects [12-14]. In some situations, quantum-dot-like nanostructures can be observed [14-16]. With different silicon doping conditions, the clustering structures are expected different. Recently, the techniques of high-resolution transmission electron microscopy (HRTEM) have been widely used for understanding the properties of threading dislocations [17,18] and nano-structures in GaN and InGaN/GaN QW samples. In particular, the existence of indium-rich clusters in InGaN/GaN QW structures has been an interesting issue of discussion [19-22]. Although some researchers claimed that the observations of clusters were due to the artifacts [19,20], created through electron beam exposure during HRTEM measurements, the existence of clusters really relies on the conditions of sample preparation. Under different conditions of crystal growth, clusters may or may not exist. Also, the cluster characteristics depend on those conditions.

In this research, we use the strain-state analysis (SSA) method [23] to study the nanostructures of InGaN/GaN QWs of different doping conditions (un-doped, well-doped, and barrier-doped) and different average indium contents. It is found that the clustering phenomenon is the strongest in the barrier-doped samples and

the weakest in the un-doped samples. Among the samples of different average indium contents, clustering behavior is relatively stronger in the high-indium samples. Based on the SSA results, the detailed nanostructures are analyzed and the relative indium contents can be confirmed. Besides, optical properties based on photoluminescence (PL) measurements are provided to show the consistent trends in the comparison of different doping conditions.

II. Sample Descriptions and Experimental Procedures

The six InGaN/GaN QW samples of different doping conditions and different average indium contents were prepared with MOCVD growth on sapphire (0001) substrate. They all consisted of five QW periods, with 2.5 nm in well width and 7.5 nm in barrier width, on top of an un-doped GaN buffer layer of 1.52 μm in thickness. The growth temperatures were 1100 and 800 $^{\circ}\text{C}$ for the GaN barriers and InGaN wells, respectively. The doping concentration of silicon was $5 \times 10^{18} \text{ cm}^{-3}$, either in barriers or wells. They are classified into two groups of low and high average indium contents. The low-indium set of samples has an estimated content of 15 %. The high-indium set has indium content of 25 % in estimation. In the low-indium set, the samples of un-doped, well-doped and barrier-doped conditions were denoted with samples LU, LW, and LB, respectively. The counterparts of the high-indium set are assigned as samples HU, HW, and HB, respectively.

The HRTEM investigations (for SSA) were performed using a Philips Tecnai F30 field-emission electron microscope using an accelerating voltage of 300 kV and a probe forming lens of $C_s = 1.2 \text{ mm}$. All the high-resolution micrographs were taken with the two-electron-beam interference. The current density focused onto the samples was estimated to be lower than 16 A/cm^2 . With the two-beam interference data, we could conduct the SSA for composition distribution images [23]. In the HRTEM operation, to avoid the possible influence of electron illumination on the recorded results [19,20], the two-beam interference images were always taken within 5-10 seconds after the electron beam was focused onto the target spots. Our experiments showed that the processed SSA images were not significantly changed within 30 seconds of the illumination of focused electron beams. To obtain the SSA images, the [0001] lattice size distributions were first calibrated from the lattice fringe images. Then, based on Vegard's law for the relation between the lattice size and indium composition, composition images could be obtained. These compositions were estimated based on the assumption of a specimen thickness larger than 50 nm. PL measurements were carried out with

the 325 nm line of a 35 mW He-Cd laser. The samples were placed in a cryostat for temperature-dependent measurements ranging from 10 to 300 K.

III. Images of Strain State Analysis

Figs. 1-6 show the typical SSA results of samples LU, LW, LB, HU, HW, and HB, respectively. In each figure, part (a) shows the lattice fringe image of two-beam interference along the [0001] direction and part (b) shows the processed SSA image. One can see that the lattice fringe image cannot clearly describe the nanostructures of materials. The colors in the SSA image represent the estimated indium composition distributions. The relationship between the lattice parameter ratio d_j/d_{GaN} (d_{GaN} and d_j for the lattice sizes of GaN and InGaN, respectively) and the indium composition x_{in} (%) is shown in the legend at the bottom of the figure. It is noted that their relationship is not linear, particularly when the indium composition is high. In each SSA image, line scan profiles of indium composition along the indicated white lines are plotted. The scales for the profiles in the two dimensions are the same. In each SSA image, a QW surrounded by the two barriers are illustrated.

Fig. 1(b) shows the SSA image of sample LU. One can see that the QW layer (green region) is quite uniform. The indium clusters (reddish regions) within the QW layer are quite small and shallow. The GaN barriers (deep blue regions) are clear. It means that indium is well confined within the well. From the horizontal line-scan profile, one can observe quite a weak fluctuation in indium composition along the well layer. The fluctuation contrast (the difference between the maximum and the minimum in the scan range) is in the range of 0.03-0.04 (18-24 %) along the QW layer. In Fig. 2(b) for sample LW, we can observe that more indium clusters are formed in the QW layer. Also, more indium atoms diffuse from the well into barriers. Here, the fluctuations of the line-scan profiles are relatively stronger in comparing with those of sample LU. The fluctuation contrast is now in the range of 0.04-0.05 (22-28 %). In Fig. 3(b) for sample LB, we can see two clear indium-rich clusters in the QW (two large red spots). From the line-scan profiles, one can see that the indium composition fluctuation in sample LB is much stronger than those of the other two samples. The fluctuation contrast is now around 0.08 (44 %).

As shown in Fig. 4(b) for sample HU, although the QW interface is blurred, indium is basically confined within the well. Here, within the well a red spot of indium aggregation can be observed. Similar to sample LU, one can also observe a

relatively weaker fluctuation in indium composition along the well layer in the line-scan profile. The fluctuation contrast is about 0.04 (22 %) along the QW layer. In Fig. 5(b) for the SSA image of sample HW, the QW is not as well shaped as sample HU. The indium composition fluctuations in both directions are relatively stronger in comparing with sample HU. In particular, more indium-aggregated clusters can be observed within the well layer. The fluctuation contrast is also around 0.04 (22 %) along the QW layer. As shown in Fig. 6(b), the SSA image of sample HB shows quite a different nanostructure from the other five samples. Here, the QW layer becomes unclear. Instead, a distribution of clusters of different sizes and shapes exists. The indium composition fluctuation is much stronger than those of samples HU and HW. The contrast is now around 0.08 (44 %) along the QW layer.

A question has been raised about the possible influence of electron beam exposure on the material nanostructures during the measurement of transmission electron microscopy [19,20]. We have tested such a possibility by varying the electron exposure time. The SSA images of sample LB shown in Figs. 7(a) and (b) were obtained under electron beam exposure for less than 10 sec and about two minutes, respectively. Fig. 7(a) is different from Fig. 3(b) because they were obtained at different locations of sample LB. Between Figs. 7(a) and (b), one can see that although the details are slightly changed, the basic structures are the same. In other words, with up to two-minute exposure, we can still obtain the required information about the nanostructures of the samples. Normally, when we operated the HRTEM system, it took less than 10 sec after the electron beam was focused onto a target spot to obtain an image. In our research, we have done our best to reduce the electron beam effect. Hence, the SSA images in this research can truly represent the sample nanostructures.

In Figs. 8 and 9, we show the average line-scan profiles in the [0001] direction, averaged over the image range along the [11-20] direction, plotted as functions of distance for the low- and high-indium samples, respectively. Two to three SSA images like Figs. 1-6 at different locations in each sample were used for taking the average. One can see that generally the well widths of the high-indium samples are larger than those of the low-indium ones. One can also observe that the interfaces between the well and barriers of the low-indium samples are generally shaper than those of the high-indium ones. Meanwhile, generally the indium concentrations at the peaks of the high-indium samples are higher than those of the low-indium ones. In addition, in the low-indium samples, more indium atoms diffuse from the well

into the lower barrier. Indium out-diffusion in the high-indium samples is more symmetric.

The average indium content of each sample can be calibrated by integrating the average line-scan results in Fig. 8 or 9 over the whole range and then dividing the integrated result by the designated QW width (2.5 nm). The whole-range integration implies the coverage of the indium atoms, which diffuse from the well into barriers. Such results of average indium content become more accurate if more SSA images like Figs. 1-6 are used for average. Although the current results cannot be very accurate, they can still be used for a general comparison. The calibrated average indium contents of samples LU, LW, and LB are 14.3, 17.1, and 19.2 %, respectively. Those of samples HU, HW, and HB are 25.6, 26.7, and 26.9 %, respectively. These results are generally consistent with the designated indium contents of 15 and 25 % for the low- and high-indium samples, respectively. The generally higher indium contents from calibration for the barrier- and well-doped samples can be attributed to the stronger indium diffusion into barriers in these two kinds of sample. With more indium atoms in the barriers, the calibration for indium composition in processing the SSA images can be overestimated. However, the possibility of really higher average indium content in the doped samples cannot be ruled out. With different strain conditions (due to different doping conditions), the incorporation efficiency of indium atom can be different even the flow rate is the same during growth.

IV. Optical Characterization Results

To understand the corresponding optical properties of these samples, basic optical characterizations were performed. Fig. 10 shows the PL spectral peak positions as functions of temperature for all the six samples with the filled and empty symbols for the low- and high-indium samples, respectively. Clear S-shape variations can be seen in the curves for samples LU and HU. On the contrary, the S-shape behaviors are unclear in the well- and barrier-doped samples. The PL peak positions of the un-doped and well-doped samples in either group of sample are quite close, particularly in the low-temperature range. The significant blue shifts of the PL peaks of samples LB and HB, with respect to those of the un-doped and well-doped samples show a clear feature of barrier doping.

Fig. 11 shows the integrated PL intensities as functions of temperature of samples LU, LW, and LB. Fig. 12 shows the counterparts of samples HU, HW, and HW. The thermal quenching behavior in integrated luminescence intensity

represents the radiative efficiency. From Figs. 11 and 12, one can see that the barrier-doped samples always have the highest radiative efficiency, followed by the well-doped samples and then the un-doped samples. Hence, in our samples, silicon doping, particularly doping in barriers, can lead to a higher efficiency of spontaneous emission.

V. Discussions

The SSA images show that barrier doping results in stronger indium clustering. This result may be caused by the significant relaxation of hetero-structure-induced strain (the strain in QW due to the lattice mismatch between wells and barriers) in the barrier-doped samples, particularly in sample HB, through certain mechanisms. In sample HB, with the growth temperature at 800 °C and nominal indium content about 25 %, the sample condition falls into the regime of spinodal decomposition (the unstable regime) in the T-x phase diagram of ternary $\text{In}_x\text{Ga}_{1-x}\text{N}$ compounds for relaxed and strained layers with the interface orientation perpendicular to the hexagonal axis of the crystal [12,24]. In this regime, spinodal decomposition and phase separation can be initiated by a small local compositional fluctuation. Hence, strongly clustering behaviors can be observed in sample HB. The mechanisms for relaxing the hetero-structure-induced strain can be the generation of local dislocations, which is caused by the enhanced lattice mismatch between a well and the surrounding barriers because of the substitutions of a high-concentration of larger gallium atoms (atomic weight as 31) by smaller silicon atoms (atomic weight as 14) in the barriers. The HRTEM images in the similar samples of our and other's previous research have shown the existence of local dislocations in an InGaN/GaN QW sample of a high nominal indium content [25,26]. The other mechanism for strain relaxation in the barrier-doped sample is the existence of plenty carriers in the barriers and wells (carriers flow into wells) due to the heavy silicon doping in the barriers. The carriers screen the piezoelectric fields and affect the strain energy distributions. However, it is believed that the major mechanism for strain relaxation is the formation of local dislocations. The discussions described above fit well the conditions of sample HB. In sample LB, because the nominal indium content is lower (about 15 %), the hetero-structure-induced strain is not as strong as that in sample HB. Therefore, the condition may fall into a region between the unstable and metastable regimes in the T-x phase diagram. In this situation, spinodal decomposition and phase separation processes can still be induced. However, these processes in the meta-stable regime take a longer time

than that in the unstable regime, leading to a relatively weaker clustering behavior.

In the well-doped samples, because of the substitutions of larger gallium or indium atoms by smaller silicon atoms (lattice mismatch reduced) and the effect of carrier screening, the hetero-structure-induced strain has been partly relaxed such that the conditions may belong to the meta-stable regime in the T-x phase diagram. Hence, certain clusters were generated although the clustering behaviors are not as strong as those in the barrier-doped samples. In the un-doped samples, the strong hetero-structure-induced strains are preserved such that the conditions are essentially located in the stable regime. In this situation, the solubility of InN in GaN is higher such that the clustering behaviors are the weakest among the three kinds of sample. It is noted that with a higher nominal indium content, the condition in the phase diagram can be closer to the meta-stable or even spinodal decomposition regime and hence the clustering behavior can be stronger.

From the SSA results above, we can build a model for potential variation along a quantum well layer. In the situations of samples HU and LU, potential fluctuations are weak. A potential minimum is surrounded by secondary minima of shallow barriers in between. In the cases of samples HW and LW, potential variations are relatively stronger. In this situation, a potential minimum is also surrounded by secondary minima. However, the barriers between the minima are now relatively higher such that certain energy is required for carrier transport between the minima. Then, for samples HB and LB, sharp minima with few secondary dips are assumed. Therefore, carriers can relax down to the absolute potential minima without a cascading process through the secondary minima. The difference between the well-doped and un-doped samples is that more energy is required for overcoming the barriers in samples LW and HW.

The relative larger PL photon energies in the barrier-doped samples can be due to the reduction of piezoelectric fields that originates from strain relaxation and carrier screening. Also, it can be due to the increase of quantum confinement, which results from the formation of nano-scale clusters. In the well-doped samples, more carriers in the well layers should result in significant increases of PL photon energies due to strong carrier screening. However, the PL photon energies of the well-doped samples are quite close to those of the un-doped samples. Such a result can be attributed to the ineffective carrier screening effect. It can also be interpreted as the result of the counteraction between band gap renormalization (red-shift trend) and piezoelectric field reduction (blue-shift trend). As shown in Fig. 10, the temperature-dependent PL spectral peak energies reveal clear S-shape

behaviors in samples LU and HU. Such an S-shape behavior is usually attributed to carrier localization [27,28] and/or QCSE [29,30]. Because the S-shape behavior is unclear in either well-doped or barrier-doped samples, whose strains are supposed to be partially or fully relaxed, the major mechanism for the S-shape behavior in our samples must be the strain distribution or QCSE. Without significant relaxation of strains in the un-doped samples, the S-shape behaviors are quite prominent. The significant enhancement of radiative recombination efficiency in the barrier-doped samples can be attributed to the strong carrier localization (localized from non-radiative recombination centers) and the reduced QCSE (improved wave function overlap between electron and hole).

VI. Conclusions

In summary, we have compared the results of SSA and PL of six InGa_N/Ga_N QW samples with un-doped, well-doped, and barrier-doped structures. Based on the SSA images, a strain relaxation model was built for describing the nanostructure differences between the three sets of sample of different doping conditions. In the barrier-doped samples, the hetero-structure-induced strains were fully relaxed such that spinodal decomposition was effectively induced. Therefore, strongly clustering nanostructures were observed. In the well-doped samples, strains were partially relaxed and the spinodal decomposition process could be slightly induced. Hence, weaker composition fluctuations were observed. Then, in the un-doped samples, the un-relaxed strains resulted in higher miscibility between In_N and Ga_N, leading to the relatively more uniform composition distributions. Between the low- and high-indium samples, higher indium content led to a stronger clustering behavior. The strain relaxations in the well-doped and barrier-doped samples resulted in their unclear S-shape behaviors of PL spectral peaks. The enhanced carrier localization and reduced QCSE in the barrier-doped samples were responsible for their significant increases of radiative efficiency.

References

1. S. Chichibu, D. A. Cohen, M. P. Mack, A. C. Abare, P. Kozodoy, M. Minsky, S. Fleischer, S. Keller, J. E. Bowers, U. K. Mishra, L. A. Coldren, D. R. Clarke, and S. P. DenBaars, *Appl. Phys. Lett.* 73 (1998) 496.
2. Y. H. Cho, J. J. Song, S. Keller, M. S. Minsky, E. Hu, U. K. Mishra, and S. P. DenBaars, *Appl. Phys. Lett.* 73 (1998) 1128.
3. M. S. Minsky, S. Chichibu, S. B. Fleischer, A. C. Abare, J. E. Bowers, E. L.

- Hu, S. Keller, U. K. Mishra and S. P. DenBaar, *Jpn. J. Appl. Phys.* 37 (1998) L1362.
4. M. Y. Ryu, Y. J. Yu, E. J. Shin, P. W. Yu, J. I. Lee, S. K. Yu, E. S. Oh, O. H. Nam, C. S. Sone, Y. J. Park, and T. I. Kim, *Solid State Communications* 116 (2000) 675.
 5. J. Dalfors, J. P. Bergman, P. O. Holtz, B. E. Sernelius, B. Monemar, H. Amano and I. Akasaki, *Appl. Phys. Lett.* 74 (1999) 3299.
 6. K. Uchida, T. Tang, S. Goto, T. Mishima, A. Niwa, J. Gotoh, *Appl. Phys. Lett.* 74 (1999) 1153.
 7. Y. C. Cheng, Cheng-Hua Tseng, Chen Hsu, Kung-Jen Ma, Shih-Wei Feng, En-Chiang Lin, C. C. Yang, and Jen-Inn Chyi, *J. Electron. Mater.* 32 (2003) 375.
 8. Y. H. Cho, F. Fedler, R. J. Hauenstein, G. H. Park, J. J. Song, S. Keller, U. K. Mishra and S. P. DenBaars, *J. Appl. Phys.* 85 (1999) 3006.
 9. S. Ruvimov, Z. Liliental-Weber, T. Suski, J. W. Ager III, J. Washburn, J. Krueger, C. Kisielowski, E. R. Weber, H. Amano and I. Akasaki, *Appl. Phys. Lett.* 69 (1996) 990.
 10. C. K. Choi, Y. H. Kwon, B. D. Little, G. H. Gainer, J. J. Song, Y. C. Chang, S. Keller, U. K. Mishra and S. P. DenBaars, *Phys. Rev. B* 64 (2001) 245339-1.
 11. M. Y. Ryu, P. W. Yu, E. Oh, C. Sone, O. Nam, and Y. Park, *Solid State Communications* 118 (2001) 547.
 12. I. Ho and G. B. Stringfellow, *Appl. Phys. Lett.* 69 (1996) 2701.
 13. Y. S. Lin, K. J. Ma, C. Hsu, S. W. Feng, Y. C. Cheng, C. C. Liao, C. C. Yang, C. C. Chuo, C. M. Lee, and J. I. Chyi, *Appl. Phys. Lett.* 77 (2000) 2988.
 14. Y. S. Lin, K. J. Ma, C. Hsu, Y. Y. Chung, C. W. Liu, S. W. Feng, Y. C. Cheng, M. H. Mao, C. C. Yang, H. W. Chuang, C. T. Kuo, J. S. Tsang, and T. E. Weirich, *Appl. Phys. Lett.* 80 (2002) 2571.
 15. Y. S. Lin, K. J. Ma, C. C. Yang, and T. E. Weirich, *J. Crystal Growth*, 242 (2002) 35.
 16. R. Seguin, S. Rodt, A. Strittmatter, L. Reissmann, T. Bartel, A. Hoffmann, D. Bimberg, E. Hahn, and D. Gerthsen, *Appl. Phys. Lett.* 84 (2004) 4023.
 17. J. Bai, T. Wang, Y. Izumi, and S. Sakai, *J. Crystal Growth* 223 (2001) 61.
 18. H. K. Cho, J. Y. Lee, C. S. Kim, G. M. Yang, N. Sharma, and C. Humphreys, *J. Crystal Growth* 231 (2001) 466.
 19. T. M. Smeeton, M. J. Kappers, J. S. Barnard, M. E. Vickers, and C. J. Humphreys, *Appl. Phys. Lett.* 83 (2003) 5419.

20. J. P. O'Neill, I. M. Ross, A. G. Cullis, T. Wang, and P. J. Parbrook, *Appl. Phys. Lett.* 83 (2003) 1965.
21. Y. C. Cheng, E. C. Lin, C. M. Wu, C. C. Yang, J. R. Yang, A. Rosenauer, K. J. Ma, S. C. Shi, L. C. Chen, C. C. Pan and J. I. Chyi, *Appl. Phys. Lett.* 84 (2004) 2506.
22. Y. C. Cheng, C. M. Wu, M. K. Chen, C. C. Yang, Z. C. Feng, G. A. Li, J. R. Yang, A. Rosenauer, and K. J. Ma, *Appl. Phys. Lett.* 84 (2004) 5422.
23. D. Gerthsen, B. Neubauer, A. Rosenauer, T. Stephan, H. Kalt, O. Schon and M. Heuken, *Appl. Phys. Lett.* 69 (1996) 2701.
24. S. Yu. Karpov, *J. Nitride Semicond. Res.* 3 (1998) 16.
25. Y. S. Lin, C. C. Yan, C. Hsu, K. J. Ma, Y. Y. Chung, S. W. Feng, Y. C. Cheng, E. C. Lin, C. C. Yang, C. T. Kuo, and J. S. Tsang, *J. Crystal Growth* 252 (2003) 107.
26. H. K. Cho, J. Y. Lee, and J. Y. Leam, *Appl. Surf. Scie.* 221 (2004) 288.
27. Y. H. Cho, G. H. Gainer, A. J. Fischer, J. J. Song, S. Keller, U. K. Mishra and S. P. DenBarrs, *Appl. Phys. Lett.* 73 (1998) 1370.
28. T. Matsuoka, H. Okamoto, M. Nakao, H. Harima, E. Kurimoto, *Appl. Phys. Lett.* 81 (2002) 1246.
29. S. F. Chichibu, A. C. Abare, M. S. Minsky, S. Keller, S. B. Fleischer, J. E. Bowers, E. Hu, U. K. Mishra, L. A. Coldren, and S. P. DenBaars, *Appl. Phys. Lett.* 73 (1998) 2006.
30. E. Berkowicz, D. Gershoni, G. Bahir, E. Lakin, D. Shilo, E. Zolotoyabko, A. C. Abare, S. P. Denbaars, and L. A. Coldren, *Phys. Rev. B* 61 (2000) 10994.

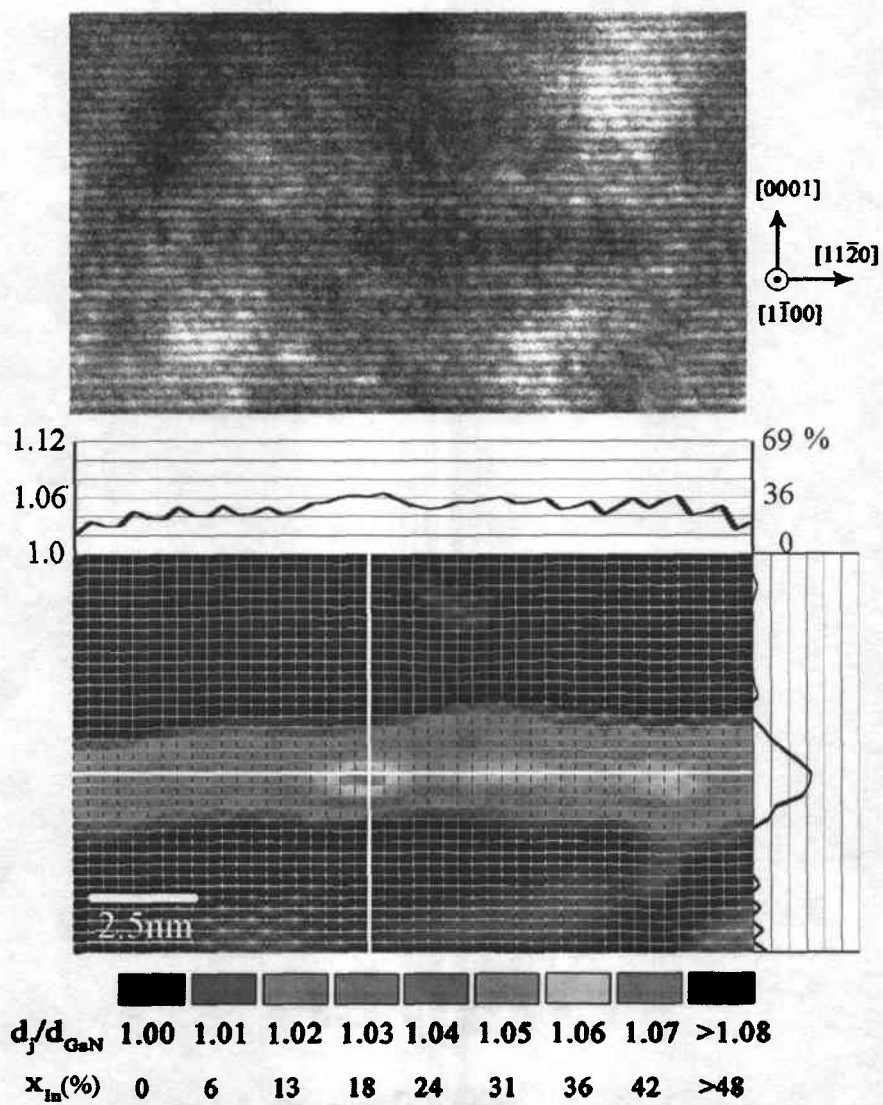


Fig. 1 Typical HRTEM lattice fringe image (a) and the SSA image (b) after software process of samples LU.

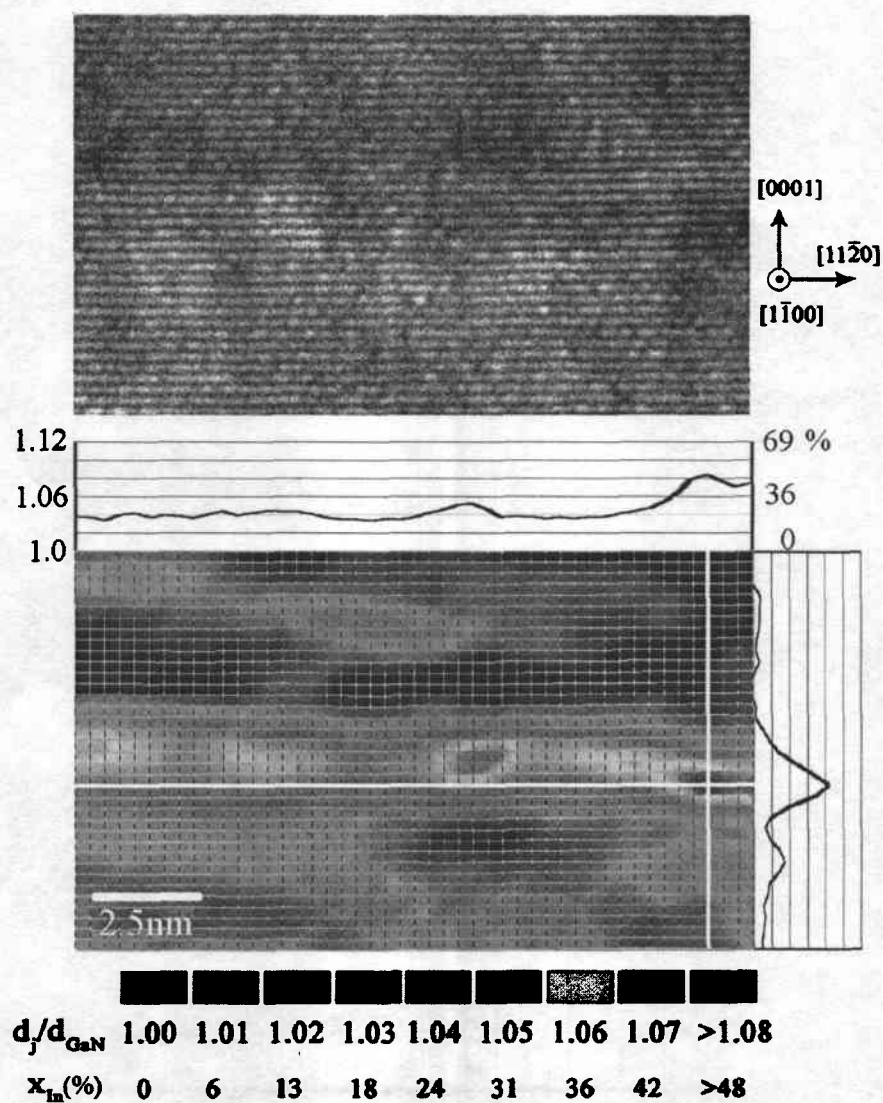


Fig. 2 Typical HRTEM lattice fringe image (a) and the SSA image (b) after software process of samples LW.

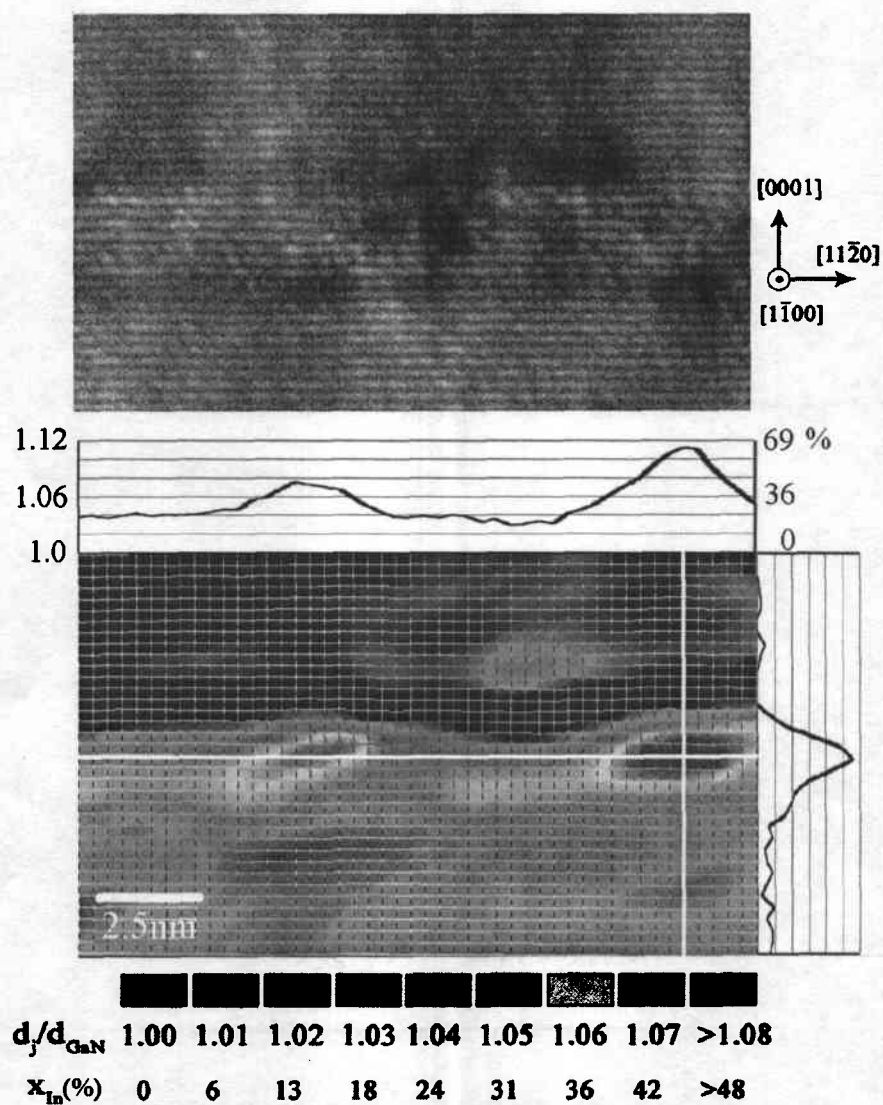


Fig. 3 Typical HRTEM lattice fringe image (a) and the SSA image (b) after software process of samples LB.

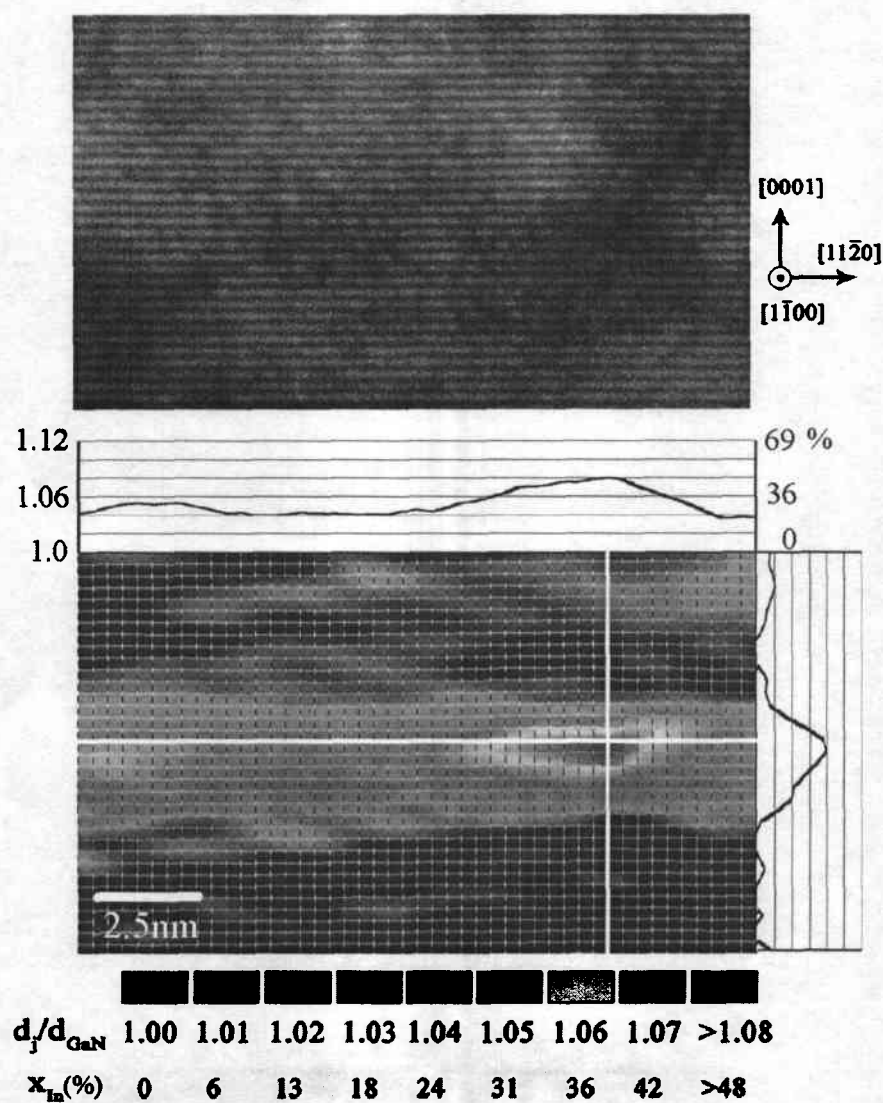


Fig. 4 Typical HRTEM lattice fringe image (a) and the SSA image (b) after software process of samples HU.

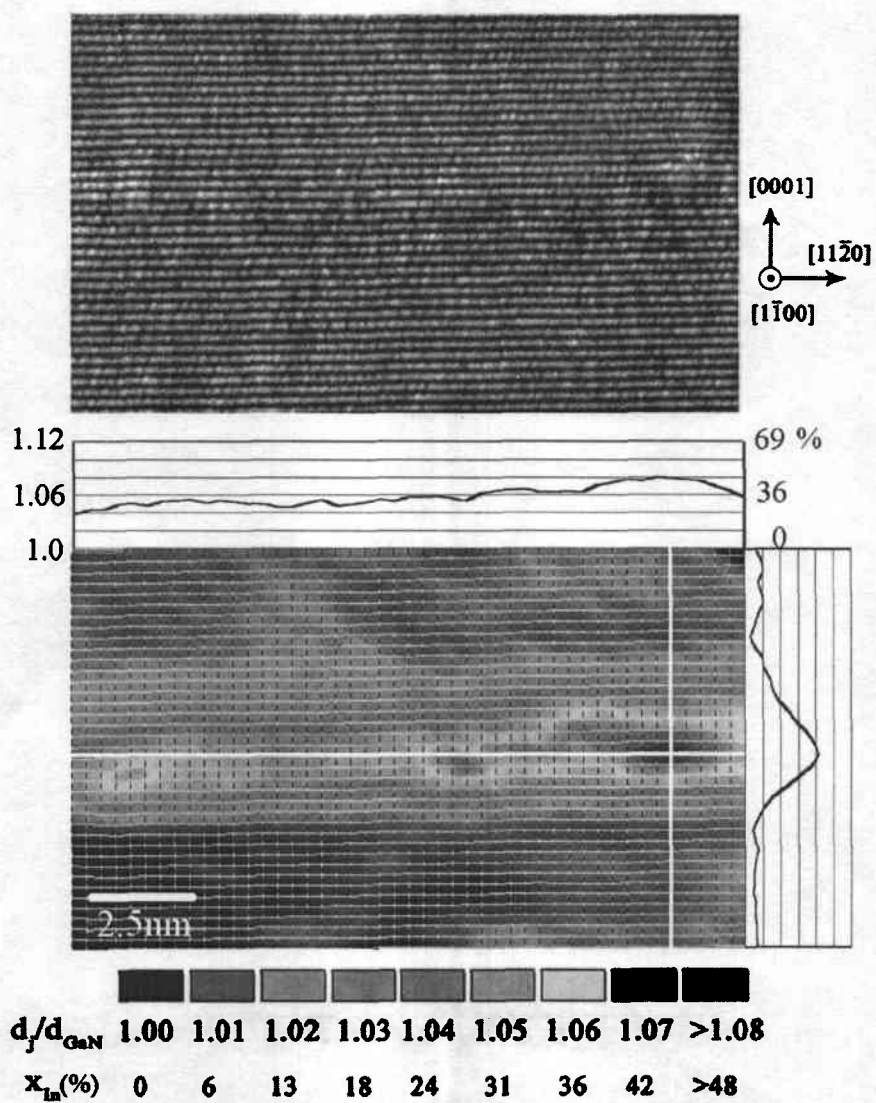


Fig. 5 Typical HRTEM lattice fringe image (a) and the SSA image (b) after software process of samples HW.

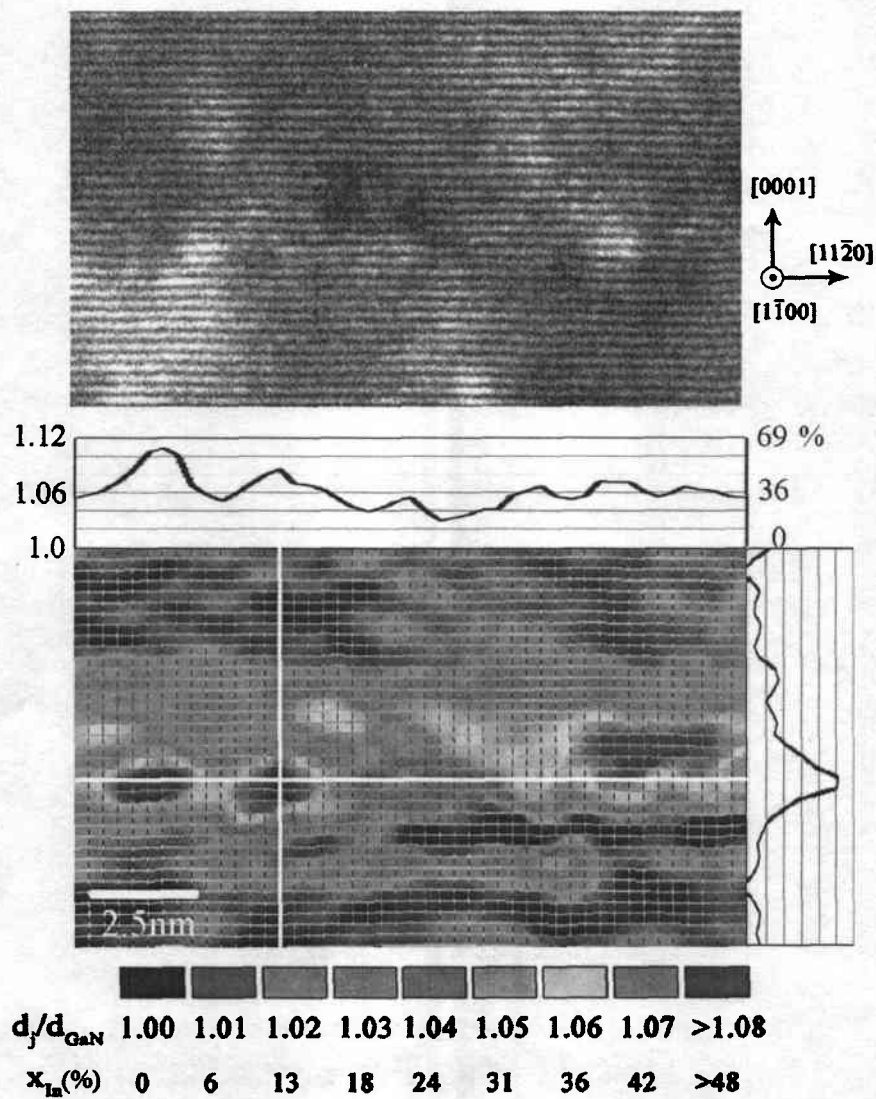


Fig. 6 Typical HRTEM lattice fringe image (a) and the SSA image (b) after software process of samples HB.

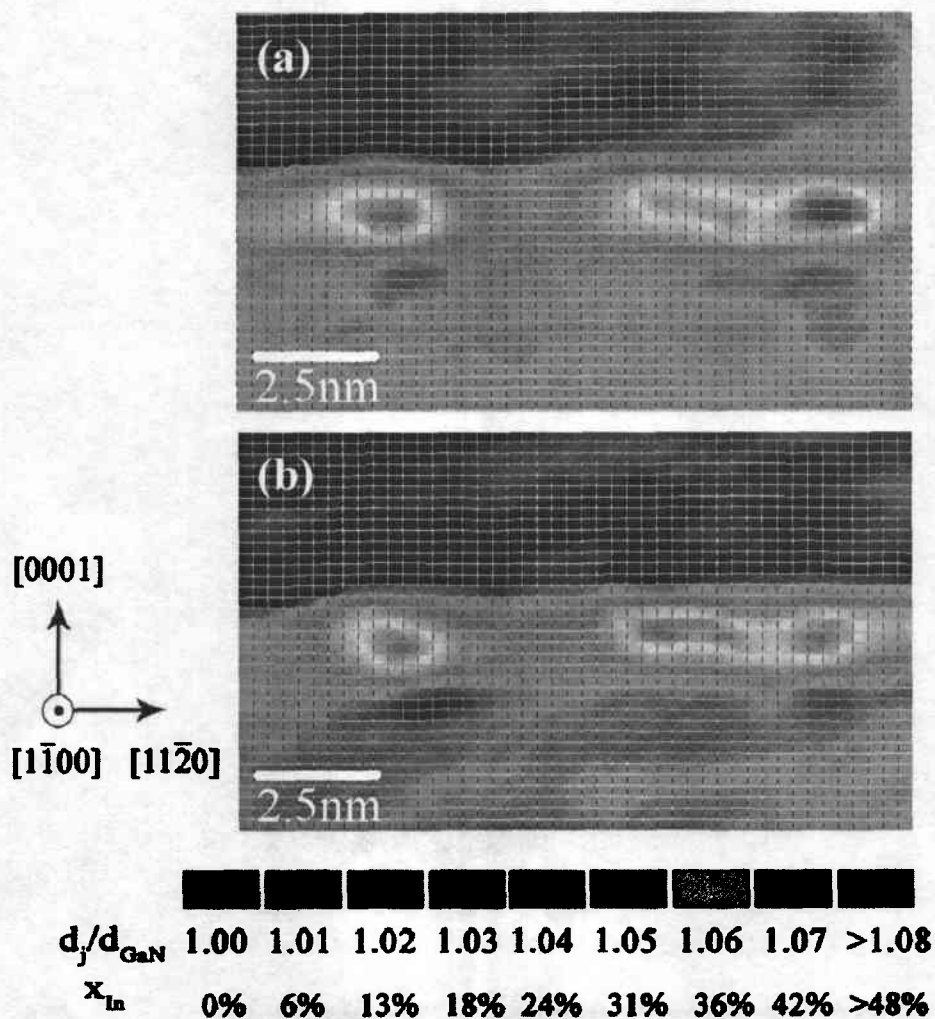


Fig. 7 SSA images of sample LB under different electron-beam exposure times: (a) <10 sec and (b) 120 sec.

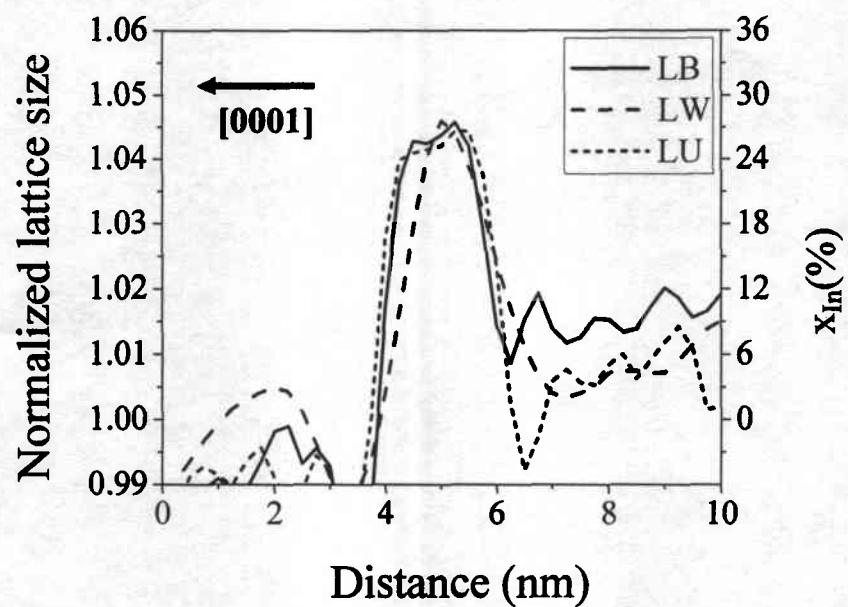


Fig. 8 Average indium composition profiles along the crystal growth direction for samples LU, LW, and LB.

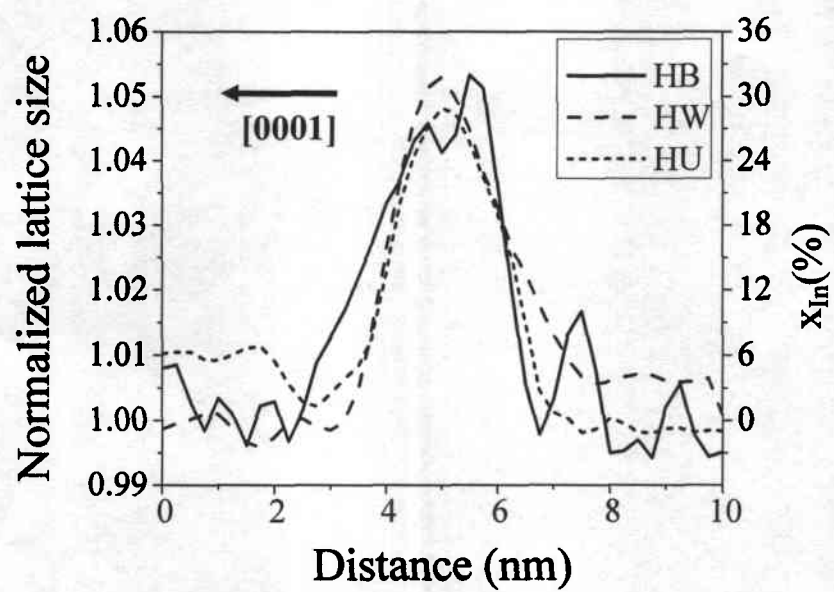


Fig. 9 Average indium composition profiles along the crystal growth direction for samples HU, HW, and HB.

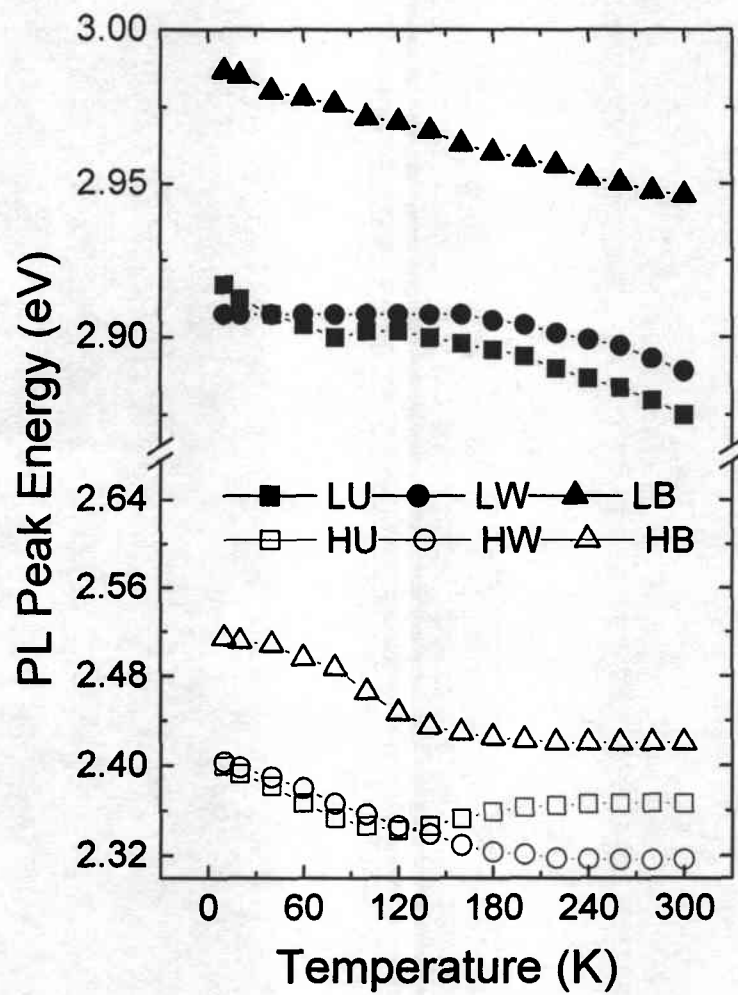


Fig. 10 PL spectral peak variations with temperature of the six samples.

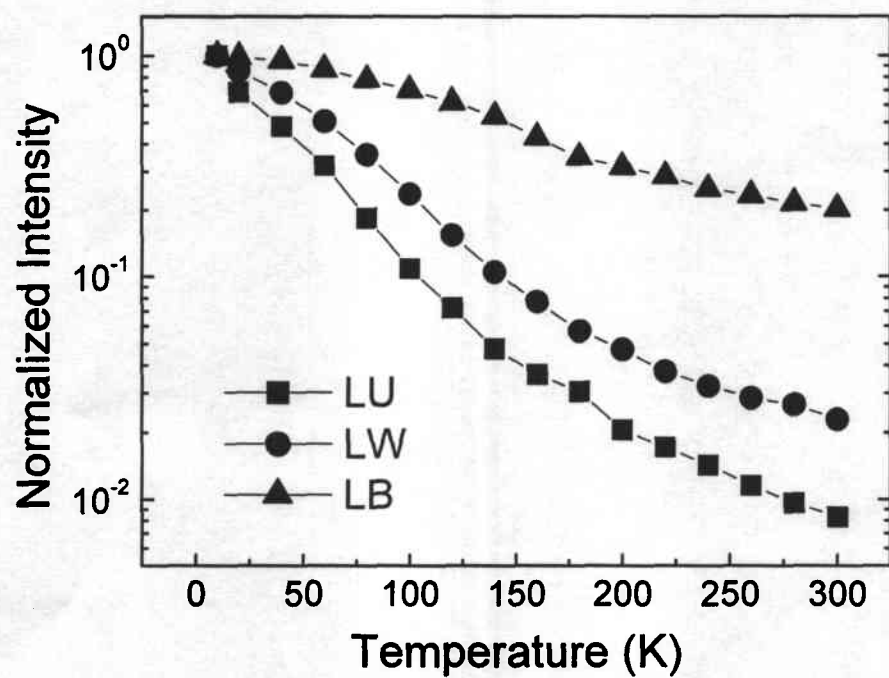


Fig. 11 Integrated PL intensity variations with temperature of samples LU, LW, and LB.

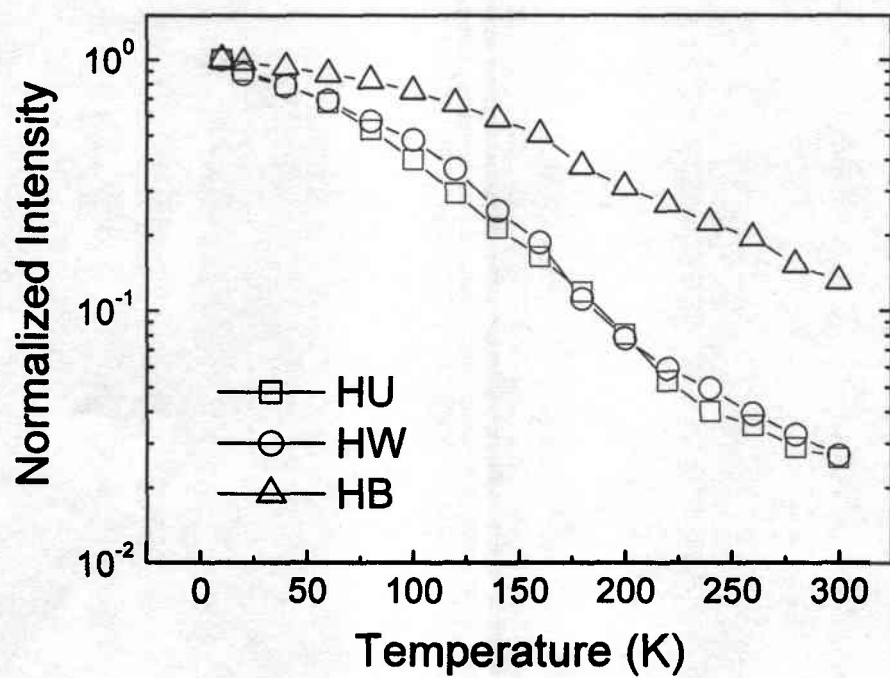


Fig. 12 Integrated PL intensity variations with temperature of samples HU, HW, and HB.

Carrier relaxation in InGaN/GaN quantum wells with nanometer-scale cluster structures

Hsiang-Chen Wang, Shih-Chun Lin, Yen-Chen Lu, Yung-Chen Cheng, and C. C. Yang^{a)}

Graduate Institute of Electro-Optical Engineering and Department of Electrical Engineering, National Taiwan University, 1, Roosevelt Road, Sec. 4, Taipei, Taiwan, Republic of China

Kung-Jen Ma

Department of Mechanical Engineering, Chung Hua University, Hsinchu, Taiwan, Republic of China

(Received 5 December 2003; accepted 18 June 2004)

Temperature-dependent femtosecond pump-probe experiments are performed to explore the ultrafast carrier-relaxation processes in an InGaN/GaN quantum-well sample, in which nanometer-scale cluster structures have been identified. Combined with the time-resolved photoluminescence results, we can identify three stages of carrier relaxation. The fast-decay time, ranging from several hundred femtoseconds to 1 picosecond, corresponds to the process reaching a local quasi-equilibrium condition, in which carriers reach a thermal distribution within one or a few nearby indium-rich clusters. The slow-decay time, ranging from tens to a couple hundred picoseconds, corresponds to the process reaching a global quasi-equilibrium condition, in which carriers reach a thermal distribution among different clusters of various potential minima. In this stage, the mechanism of carrier transport over barriers between clusters dominates the relaxation process. Finally, carrier recombination dominates the relaxation process with the carrier lifetime in the range of a few nanoseconds. © 2004 American Institute of Physics. [DOI: 10.1063/1.1784033]

InGaN/GaN quantum-well (QW) structures have been widely used for blue-green light-emitting devices. Due to the large lattice mismatch between InN and GaN, indium-rich aggregation usually occurs in InGaN, leading to the formation of nanometer-(nm)-scale clusters and hence potential fluctuations.^{1–6} Carriers, once generated, are trapped in the localized states of potential minima and recombine effectively. The cluster structure is the key to the efficient emission in such a compound. Normally, cluster structures with well-defined potential minima, such as those in a sample of barrier doping with silicon, result in higher emission efficiency.⁷ Because the information of carrier relaxation in such a sample can help us in understanding better its nanostructure and hence the recombination process, an ultrafast pump-probe study is useful for the development of related devices. Although a temperature-dependent femtosecond (fs) pump-probe experiment on InGaN/InGaN QWs of low indium contents was reported,⁸ no cluster-related phenomena were mentioned.

In this letter, we report the results of temperature-dependent fs pump-probe experiments on an InGaN/GaN QW sample. By combining the results of picosecond-scale time-resolved photoluminescence (TRPL) measurement, we can identify different time scales of carrier relaxation process. The sample consists of five periods of QW with 2.5 nm In_{0.15}Ga_{0.85}N wells and 10 nm GaN barriers. The details of sample structure and growth condition can be found in Ref. 9. Cluster structures in the nm scale have been identified in this sample with high-resolution transmission electron microscopy.¹⁰ In the pump-probe experiment, a 76 MHz, 100 fs Ti:sapphire laser, pumped with a Nd:YVO₄ laser, was frequency doubled through a 0.5-mm-thick BBO crystal. The second-harmonic pulses were split into two beams for degen-

erate, noncollinear, and cross-polarized pump-probe measurements. A half-wave plate and two polarizers were used to minimize coherent artifacts. The 1 μ m stepping resolution of the computer-controlled translation delay stage accounts for 7 fs step size in the time domain. Pump photon energies at 2.98 and 3.14 eV were chosen, as explained in the following, with average powers at 12 and 32 mW (4.96 and 13.2 μ J/cm²), respectively. The sample was back-side polished to guarantee effective transmission of the probe beam. Figure 1 shows the photoluminescence (PL) and photoluminescence excitation (PLE) spectra at 10 K. At around 3.14 eV, there is an absorption peak in the PLE spectrum. Also, near 2.98 eV, the PLE intensity reaches its minimum before it rapidly increases as the photon energy falls into the PL spectral range. We choose these two photon energies for pumping the sample (see the arrows in Fig. 1).

In Fig. 2, we show the differential transmission, $\Delta T/T$, as functions of time at various sample temperatures when the

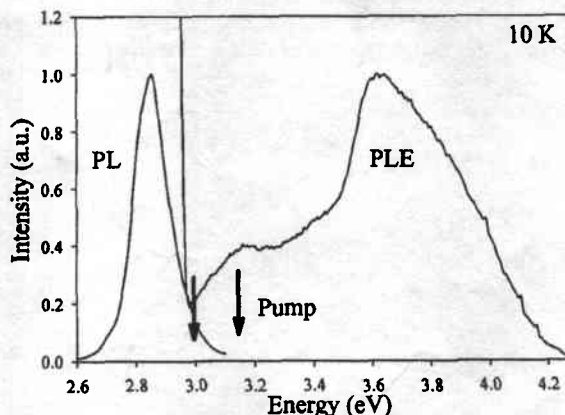


FIG. 1. PL and PLE spectra at 10 K. The used pump photon energies are indicated with arrows.

^{a)}Electronic mail: ccy@cc.ee.ntu.edu.tw

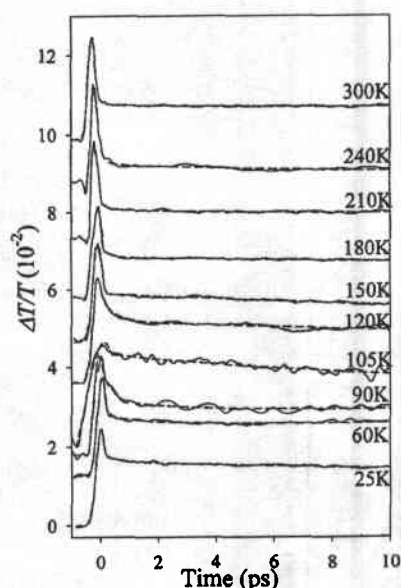


FIG. 2. Time evolution of differential transmission at various sample temperatures when the pump energy is 2.98 eV.

pump-probe photon energy is 2.98 eV. One can see that in each temporal trace, after the pump pulse, differential transmission decays with time first quite fast in the fs range, followed by a slower picosecond- (ps)-scale decay. Traces in Fig. 2 show the temperature-dependent variations of the fast-decay speed and relative level of the slow-decay range. The decay behavior around 105 K is quite different from those at lower or higher temperatures. In particular, oscillations in the slow-decay range can be clearly seen. Such oscillations are supposed to be due to the existence of coherent acoustic phonons.^{11,12}

To explore the decay phenomena, we evaluated the ratio of differential transmission of the level in the slow-decay range (we used the value at 4 ps to represent this level) over that of the peak. The results are shown in the curve with closed triangles in Fig. 3. The vertical line segments represent the error bars, which were obtained from ten times measurements. Also shown in Fig. 3 is the curve with closed circles for the PL spectral peak position as a function of temperature. The PL spectral peak position shows a typical S-shape variation, which is a key feature of a clustering structure, indicating the effect of carrier localization.^{9,13,14} In

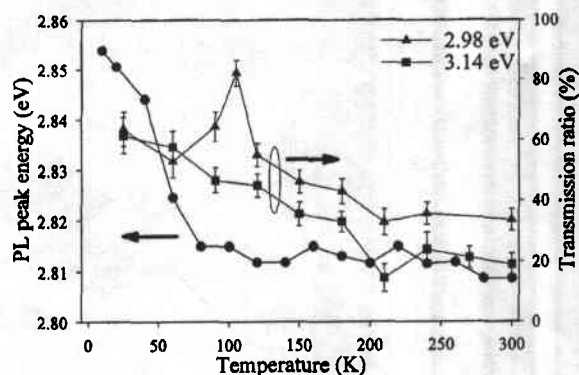


FIG. 3. Temperature-dependent variations of PL spectral peak and transmission ratios at two pump energies.

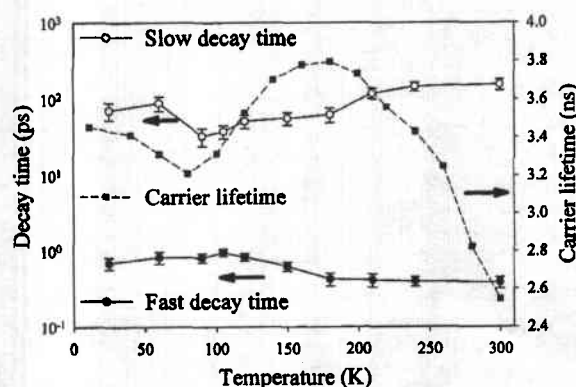


FIG. 4. Temperature-dependent variations of the fast- and slow-decay times and the carrier lifetime when the pump energy is 2.98 eV.

Fig. 3, it is interesting to observe that when the sample is pumped with photon energy of 2.98 eV, a peak of transmission ratio exists around 105 K, at which the PL spectral peak starts to show the significant blueshift trend. Based on the observation, we can build a model as follows: At low temperatures (<105 K), the pump photon energy is far above the peak level of carrier thermal distribution. In this situation, once carriers are generated, in the process of approaching the quasi-equilibrium condition, carriers move rapidly into the states of lower levels. Therefore, after the fast decay, the carrier density at the pump energy level is low. When temperature increases to a certain level (around 105 K in this sample), the peak level of carrier thermal distribution is raised to become close to the pump energy level. In this situation, plenty of carriers stay in the levels close to the pump energy during the relaxation process of approaching a quasi-equilibrium condition. Therefore, the transmission ratio shown in Fig. 3 reaches a maximum around 105 K. Beyond this temperature, the phonon effect (leading to band gap shrinkage in increasing temperature) gradually dominates and the peak level of carrier distribution moves below the pump energy level. Hence, the transmission ratio essentially decreases with temperature.

To obtain the carrier decay times, we used a model of double-exponential variation, convolved with a Gaussian function (the pump pulse), to fit the measured data,¹⁵ as illustrated by the dashed curves in Fig. 2. With such fitting, the fast- and slow-decay times were obtained, as plotted in Fig. 4. One can see that the fast decay times (closed circles) are in the range from 700 fs to 1 ps. It generally decreases with temperature with a shallow maximum around 105 K. On the other hand, the slow-decay times (open circles) range from 50 to 200 ps with a general increasing trend with temperature. A minimum around 105 K can be clearly seen. In Fig. 4, we also show the carrier lifetimes, which were obtained with TRPL measurement by using a streak camera of about 4 ps in temporal resolution. They were calibrated from the nanosecond- (ns)-scale decay of PL intensity when the sample was excited with 100 fs pulses at 3.14 eV. These decay times are in the range of a few ns and correspond to the carrier lifetime in the recombination process. In the TRPL measurement, a faster decay with decay time in the ps range was also observed. This ps-scale decay, corresponding to the open-circle data in Fig. 4, has been attributed to the carrier transport process among potential minima of different levels.¹⁶ With such observations, we can speculate that the

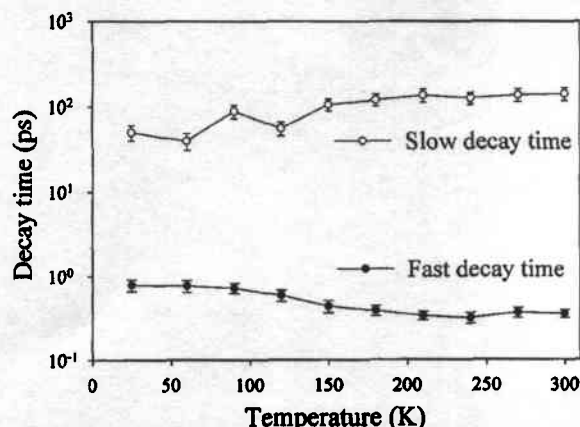


FIG. 5. Temperature-dependent variations of the fast- and slow-decay times when the pump energy is 3.14 eV.

fast-decay times in Fig. 4 describe the carrier relaxation process toward a quasi-equilibrium condition in a localized region (within one or a few nearby clusters). Because the sample has a structure between two and zero dimensions, a quasi-continuous state distribution still exists. Hence, carrier redistribution among different states for a local quasi-equilibrium condition dominates carrier dynamics in this time range. Such a process becomes faster as temperature increases, as clearly described in Fig. 4. After this stage, carriers significantly transport to neighboring clusters of higher or lower potential minima, reaching a global quasi-equilibrium condition. This process takes an average time of about 100 ps, which is consistent with our previous calibrations based on the TRPL measurement.⁹ At the temperature (around 105 K) where the PL spectral peak shows a significant blue shift, such a relaxation process becomes faster because carriers are supposed to move into the energy states close to the pump level. In this transport process, carriers need to gain certain thermal energy for overcoming the barriers between neighboring clusters. After the transport stage, electrons with the global quasi-equilibrium condition will eventually relax back to the valence band with a time scale of carrier lifetime.

With pump at 3.14 eV, the transmission ratios are shown as the curve with closed squares in Fig. 3. In this situation, the peak around 105 K, like that in the case of 2.98 eV pump, disappears. The result is attributed to the fact that the pump energy is far above the peak level of thermal carrier distribution, even with the blueshift trend of PL spectral peak beyond 105 K. The fitted fast- and slow-decay times in the case of 3.14 eV pump are shown in Fig. 5. The results are similar to those in Fig. 4 although the decay times with 3.14 eV pump are slightly shorter. It has been pointed out that the carrier transport process through overcoming a vari-

ety of barrier heights should follow a power-law behavior in time evolution.¹⁷ However, because our measurement time range (~ 10 ps) represents only a small portion of the whole slow-decay process, it is difficult to exactly calibrate its time dependence.

In summary, we have performed temperature-dependent, fs pump-probe experiments to explore the ultrafast carrier-relaxation processes in an InGaN/GaN QW sample, in which nm-scale cluster structures have been identified. Combined with the TRPL results, we could identify three stages of carrier relaxation. The fast-decay time, ranging from several hundred fs to 1 ps, corresponded to the process toward a local quasi-equilibrium condition, in which carriers reached a thermal distribution within one or a few nearby clusters. The slow-decay time, ranging from tens to a couple of hundred ps, corresponded to the process toward a global quasi-equilibrium condition. Finally, the mechanism of carrier recombination dominated the process with the carrier lifetime in the range of a few ns.

This research was supported by National Science Council, The Republic of China, under Grant Nos. NSC 92-2210-M-002-006 and NSC 92-2215-E-002-010, and by US Air Force under Contract No. AOARD-04-4026.

¹S. Chichibu, T. Sota, and S. Nakamura, *Appl. Phys. Lett.* **71**, 2346 (1997).

²Y. Narukawa, Y. Kawakami, M. Funato, Sz. Fujita, Sg. Fujita, and S. Nakamura, *Appl. Phys. Lett.* **70**, 981 (1997).

³M. D. McCluskey, L. T. Romano, B. S. Krusor, D. B. Bour, N. M. Johnson, and S. Brennan, *Appl. Phys. Lett.* **72**, 1730 (1998).

⁴Y. S. Lin, K. J. Ma, C. Hsu, S. W. Feng, Y. C. Cheng, C. C. Liao, C. C. Yang, C. C. Chuo, C. M. Lee, and J. I. Chyi, *Appl. Phys. Lett.* **77**, 2988 (2000).

⁵Y. S. Lin, K. J. Ma, C. Hsu, Y. Y. Chung, C. W. Liu, S. W. Feng, Y. C. Cheng, M. H. Mao, C. C. Yang, H. W. Chuang, C. T. Kuo, J. S. Tsang, and T. E. Weirich, *Appl. Phys. Lett.* **80**, 2571 (2002).

⁶S. W. Feng, Y. C. Cheng, H. C. Wang, C. C. Yang, C. H. Shen, L. C. Chen, K. J. Ma, J. Y. Lin, and H. X. Jiang, *Appl. Phys. Lett.* **83**, 3906 (2003).

⁷Y. C. Cheng, C. H. Tseng, C. Hsu, K. J. Ma, S. W. Feng, E. C. Lin, C. C. Yang, and J. I. Chyi, *J. Electron. Mater.* **32**, 375 (2003).

⁸A. Satake and Y. Masumoto, *Phys. Rev. B* **60**, 16660 (1999).

⁹Y. Y. Chung, Y. S. Lin, S. W. Feng, Y. C. Cheng, E. C. Lin, C. C. Yang, K. J. Ma, C. Hsu, H. W. Chuang, C. T. Kuo, and J. S. Tsang, *J. Appl. Phys.* **93**, 9693 (2003).

¹⁰Y. S. Lin, K. J. Ma, C. C. Yang, and T. E. Weirich, *J. Cryst. Growth* **242**, 35 (2002).

¹¹A. V. Kuznetsov and C. J. Stanton, *Phys. Rev. B* **51**, 7555 (1995).

¹²C. K. Sun, J. C. Liang, and X. Y. Yu, *Phys. Rev. Lett.* **84**, 179 (2000).

¹³Y. H. Cho, G. H. Gainer, A. J. Fischer, J. J. Song, S. Keller, U. K. Mishra, and S. P. DenBaars, *Appl. Phys. Lett.* **73**, 1370 (1998).

¹⁴P. G. Eliseev, P. Perlin, J. Lee, and M. Osinski, *Appl. Phys. Lett.* **71**, 569 (1997).

¹⁵Ö. Özgür, H. O. Everitt, S. Keller, and S. P. DenBaars, *Appl. Phys. Lett.* **82**, 1416 (2003).

¹⁶S. W. Feng, Y. Y. Chung, C. W. Liu, Y. C. Cheng, C. C. Yang, M. H. Mao, Y. S. Lin, K. J. Ma, and J. I. Chyi, *Appl. Phys. Lett.* **80**, 4375 (2002).

¹⁷S. Y. Grabtchak and M. Cocivera, *J. Appl. Phys.* **79**, 786 (1996).

Ultrafast carrier dynamics in an InGaN thin film

Hsiang-Chen Wang, Yen-Cheng Lu, Chih-Chung Teng, Yung-Sheng Chen, and C. C. Yang^{a)}

Graduate Institute of Electro-Optical Engineering and Department of Electrical Engineering, National Taiwan University, 1, Roosevelt Road, Sec. 4, Taipei, Taiwan 106, Republic of China

Kung-Jen Ma

Department of Mechanical Engineering, Chung Hua University, Hsinchu, Taiwan 300-71, Republic of China

Chang-Chi Pan and Jen-Inn Chyi

Department of Electrical Engineering, National Central University, Chung-Li, Taiwan 320, Republic of China

(Received 8 July 2004; accepted 9 November 2004; published online 6 January 2005)

We perform femtosecond degenerate pump-probe experiments on an InGaN thin film of 800 nm in thickness. The observed temperature-, pump-photon-energy-, and pump-intensity-dependent variations of ultrafast carrier dynamics manifest the variation of the space-averaged density of state with energy level in this sample. The carrier dynamics is controlled by the shift of effective band gap and hence the behavior of band filling, which are determined by the combined effect of band-gap renormalization and phonon effect (band-gap shrinkage with increasing temperature). Two-photon absorption and free-carrier absorption can be observed when the corresponding density of state is low and hence the band-filling effect is weak. The variation of the space-averaged density of state with energy level can be due to the existence of indium-composition-fluctuation nanostructures, which is caused by the spinodal decomposition process, in the sample. © 2005 American Institute of Physics. [DOI: 10.1063/1.1847705]

I. INTRODUCTION

Because of the large lattice mismatch between GaN and InN, two important phenomena in InGaN compounds have been widely observed, including indium-composition fluctuation (or clustering)¹⁻⁴ and strain-induced piezoelectric field near an interface of a heterostructure.⁵⁻⁹ The former leads to carrier (exciton) localization and hence radiative efficiency improvement. The latter results in quantum-confined Stark effect (QCSE) and hence carrier separation in a carrier-confined structure. Both phenomena are important in interpreting the photon emission mechanisms in such a compound. In particular, these two phenomena interplay in an InGaN/GaN quantum well (QW) structure, leading to complicated optical behaviors. Normally, when the heterostructure-induced strain is relaxed through a certain process, spinodal decomposition can be easily induced such that indium composition fluctuations and indium-rich clusters can be formed in such a sample.^{10,11} On the other hand, if the strain is preserved, the solid miscibility between InN and GaN can be increased such that relatively more uniform InGaN ternary compounds can exist. In this situation, higher QW quality can be obtained.

With the effects of carrier localization and QCSE mixed in a QW sample, it is usually difficult to identify either effect clearly. However, in an InGaN thin-film sample of large enough thickness (larger than the critical thickness), the strain effect can be relaxed in most part of the sample. In this situation, we can exclude the QCSE and observe the effect in

the optical property of potential fluctuation solely. To understand the photon emission mechanisms of such a material, ultrafast carrier dynamics observed with femtosecond pump-probe experiments have been proven an effective tool.^{12,13} Carrier flow information can help us in understanding the nanostructures, which provide us with the clues for light-emission origins. In this paper, we report the results of ultrafast carrier dynamics in an InGaN thin film with the thickness larger than the critical thickness, particularly near the energy levels of free-carrier states. Temperature-, pump-photon-energy-, and pump-intensity-dependent femtosecond degenerate pump-probe differential transmission traces show significant variations of important implications. Such variations are attributed to the variation of the space-averaged density of state, which is due to the indium-composition fluctuation in the sample. This paper is organized as follows: Descriptions of the sample structure and experimental methods are presented in Sec. II. The pump-probe experimental results are discussed in Sec. III. More discussions are given in Sec. IV. Finally, conclusions are drawn in Sec. V.

II. SAMPLE PREPARATION AND EXPERIMENTAL METHODS

The InGaN thin-film sample was grown on *c*-plane sapphire with metal-organic chemical-vapor deposition (MOCVD). After the 800-nm GaN buffer layer, an 800-nm InGaN thin film with silicon doping of $5 \times 10^{18} \text{ cm}^{-3}$ in concentration was grown at 800 °C. The average indium content was estimated to be 20%. Because the critical thickness of InGaN under the current conditions is only about 50 nm,¹⁴

^{a)}FAX: 886-2-2365263; electronic mail: ccy@cc.ee.ntu.edu.tw

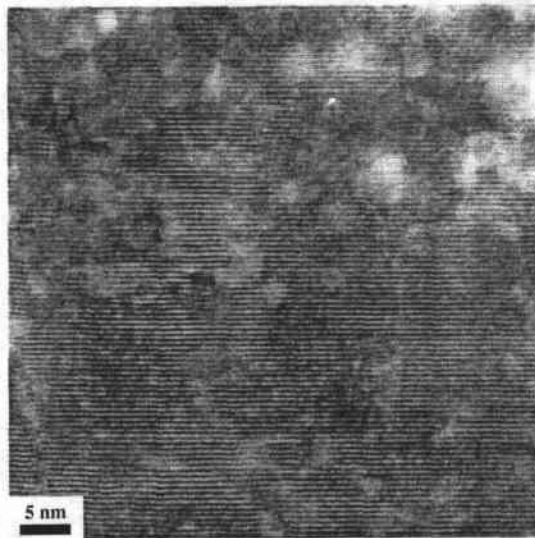


FIG. 1. A HRTEM image of the sample.

the results of transmission measurement mainly originate from the strain-relaxed portion of InGa_N. However, composition fluctuations of roughly 10 nm in scale size were observed in the sample with high-resolution transmission electron microscopy (HRTEM), as shown in Fig. 1. The bright regions in the HRTEM image represent the indium-rich distributions. The HRTEM investigation was performed using a Philips TECNAI F20 field-emission electron microscope with an accelerating voltage of 200 kV. The high-resolution micrograph was taken at the Scherzer defocus. The sample was viewed along a $^{11-20}$ zone axis for a bright-field image.

In the optical experiment, the degenerate pump and probe sources originated from the second-harmonic of a mode-locked Ti:sapphire laser with a beta barium borate (BBO) crystal. The second-harmonic pulse width was about 150 fs. The tuning range was from 2.7 through 3.4 eV. The average power for the pump ranged from 4 through 42 mW. That for the probe was fixed at 0.5 mW. In the temperature-dependent measurements, the pump average power was fixed at 9 mW. The pump-probe light spot on the sample surface was about 0.1 mm in diameter.

III. PUMP-PROBE EXPERIMENTAL RESULTS

Figure 2 shows the temperature-dependent variation of photoluminescence (PL) spectra and the spectral peak positions as functions of temperature. Two PL spectral peaks are identified below 200 K. An S-shaped variation for the low-energy peak can be clearly seen. Such a variation has been regarded as one of the optical features of indium-rich clusters in the InGa_N thin film.^{3,15} The low-energy peak corresponds to the localized states. The high-energy peak is attributed to the free-carrier states, corresponding to the background InGa_N compound, on which clusters are distributed. However, it is noted that the background InGa_N compound also consists of potential fluctuations of shallower distributions. The merge of the two PL peaks above 200 K is attributed to carrier liquidation among the

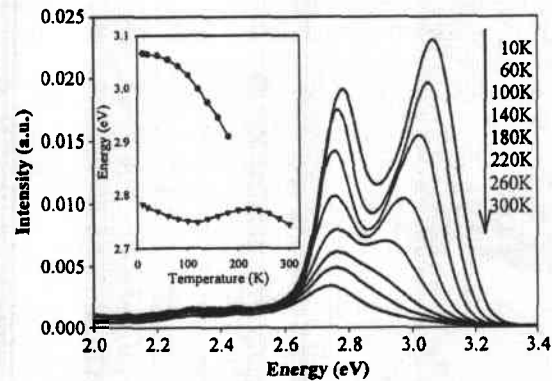
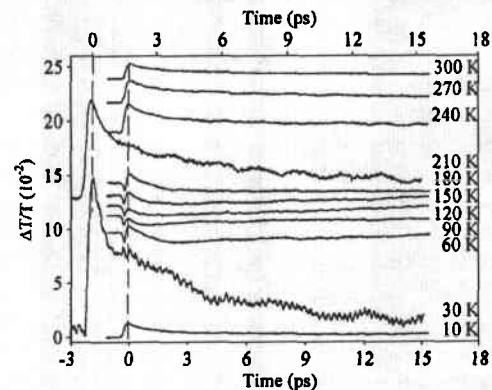


FIG. 2. Temperature-dependent PL spectra and the calibrated spectral peak positions for the high and low energy peaks.

localized states and free-carrier states. The decreasing trend of the high-energy peak is mainly due to the band-gap shrinkage of phonon effect. The concerned photon energy range in our pump-probe experiments is close to the high-energy peak of PL spectrum. In other words, we are interested in the carrier dynamics at the energy levels around free-carrier states.

Figure 3 shows the differential transmission ($\Delta T/T$) traces of various temperatures with the pump photon energy at 3.2 eV. The time-resolved traces show quite different behaviors as temperature increases from 10 through 300 K. Below 30 K, after the strong pump-induced peak, the probe intensity decays with a double-exponential profile within 15 ps. The pump-induced peak at 30 K is particularly strong (up to 14%), indicating the strong band-filling effect at this temperature. However, between 60 and 180 K, the pump-induced probe intensity shows a sharp decrease first and then an increase to a certain level. This level is lower than that of negative delay (without pump) in either trace of 90 and 120 K. In this temperature range, the $\Delta T/T$ variation is the weakest among the traces in Fig. 3. In the temperature range between 60 and 180 K, the probe intensity decreases and then increases from the peak of the aforementioned level. In some of these traces, the levels around 15 ps are higher than those

FIG. 3. Differential transmission traces of different sample temperatures with pump photon energy at 3.2 eV. The pump pulse energy density is $3.26 \mu\text{J}/\text{cm}^2$. Two zero delay times for different traces are shown with the vertical dashed lines.

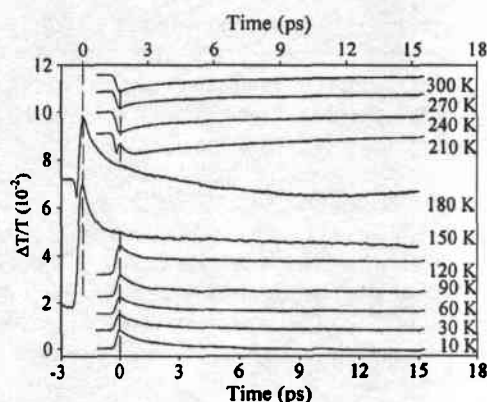


FIG. 4. Differential transmission traces of different sample temperatures with pump photon energy at 3.14 eV. The pump pulse energy density is $3.26 \mu\text{J}/\text{cm}^2$.

of negative delay. As temperature increases beyond 180 K, the behavior of double-exponential decay from the pump-induced peak reappears. The peak level reaches another maximum (about 9%) around 210 K. In the traces of 30 and 210 K, quasiperiodical oscillations can be observed. Such oscillations correspond to a frequency of 0.54 THz. They are attributed to the interaction of coherent acoustic phonon.^{16–18} Such coherent phonon interaction is expected at all temperatures; however, we can observe it only at those of significant band-filling effects. The acoustic phonon is created at the incidence of the pump laser. In a multiple QW sample, it travels through the sample and interacts with the carriers in the wells. Therefore, the oscillation period of the pump-probe trace corresponds to the period of the QW.¹⁸ In our case, by assuming that the acoustic speed in the InGa_{0.53}N thin film is 6000 m/s,¹⁸ the observed oscillations of around 0.54 THz correspond to a periodical structure of 11 nm in period. In the used sample, although composition fluctuations are observed in the HRTEM image (see Fig. 1), we have no strong evidence for this periodical structure. However, there is no reason to exclude such a possibility either. This scale size (around 11 nm) may represent a characteristic dimension of the indium-rich clusters or composition fluctuations. Nevertheless, it deserves further investigation.

Figure 4 shows the $\Delta T/T$ traces at various temperatures with the pump photon energy at 3.14 eV. Here, one can observe the behavior of double-exponential decay after the pump-induced peak in the temperature range below 180 K. Above this temperature, the behavior of the probe intensity decrease at the pump instant can be seen. The trace of 210 K is similar to that of 120 K in Fig. 3. However, above this temperature, the small feature rise after the dip disappears. Here, a double-exponential rising behavior can be observed.

To summarize the data in Figs. 3 and 4, and the similar results of other pump photon energies, the photoinduced change of optical density (ΔOD) versus temperature at three pump-probe photon energies is shown in Fig. 5.¹⁹ The optical density is defined as the ratio of unpumped transmission over the pumped transmission in the log scale at zero pump-probe delay, i.e., the temporal positions indicated with the vertical dashed lines in Figs. 3 and 4. In Fig. 5, variations of ΔOD of

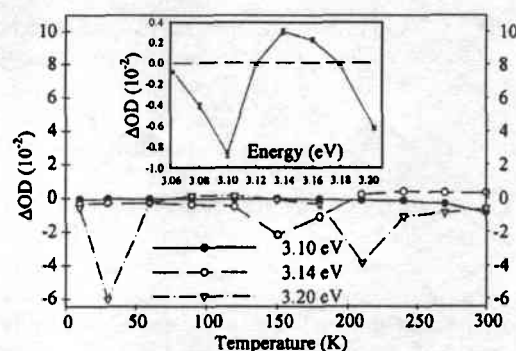


FIG. 5. ΔOD vs temperature of three pump photon energies and ΔOD vs photon energy at room temperature.

different amplitudes for the three photon energies can be observed. In the inset of Fig. 5, ΔOD data versus photon energy at room temperature are plotted. Here, a quasiperiodical variation with a period around 120 meV can also be seen.

Figure 6 shows the $\Delta T/T$ traces of various pump pulse energy densities (equivalent to pump intensities) at room temperature with the pump photon energy at 3.1 eV. One can see that as the pump pulse energy density increases from $2.89 \mu\text{J}/\text{cm}^2$ (corresponding to $1.94 \times 10^{17} \text{ cm}^{-3}$ photogenerated carrier density) to $16.53 \mu\text{J}/\text{cm}^2$, the $\Delta T/T$ profile changes from the pattern of single hump into that of a dip.

IV. DISCUSSIONS

$\Delta T/T$ represents the transient absorption alteration of the probe upon the pump excitation. A trace with a rise, followed by a double-exponential decay (including the faster local carrier thermalization plus carrier relaxation into lower energy levels and the slower carrier diffusion or global carrier thermalization¹⁷), is normally interpreted as the band-filling effect, which diminishes with the carrier flow and recombination. In such a process, band-gap renormalization and phonon effect can also occur. With a high localized-carrier density upon the pump excitation, band-gap renormalization leads to a reduced band gap. This process combines with the phonon effect for the resultant effective band-gap alteration.

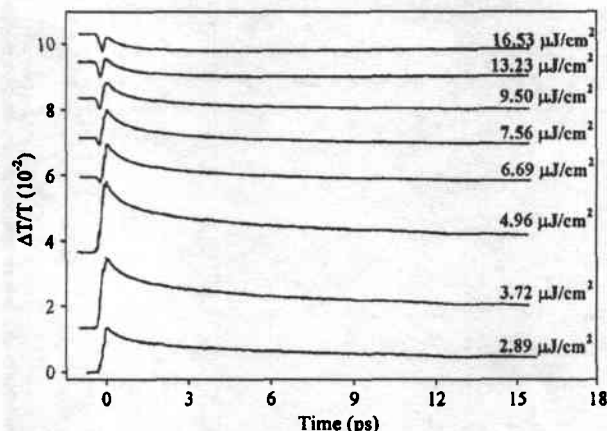


FIG. 6. Differential transmission traces of different pump photon energy densities at room temperature with the pump photon energy at 3.1 eV.

When the band gap varies, the pump-probe photon corresponds to the energy levels of different space-averaged densities of state, which determine the band-filling processes and hence the $\Delta T/T$ behaviors. Therefore, the variations of the $\Delta T/T$ behavior, in changing either temperature, pump photon energy, or pump intensity, should follow the variation pattern of the space-averaged density of state along the energy level. Here, the space-averaged density of state means the average energy-level density over a spatial region of composition fluctuations. In this region, because of the spatial potential variation, random or organized, space-averaged density of state may show strong dependence on the energy level. A quasiperiodical variation can exist in such a structure formed through spinodal decomposition. As shown in Figs. 3 and 4, when temperature increases, the band gap shrinks and the pump-probe photon energy moves to the higher energy level with respect to the band edge. In this situation, the pump may experience different densities of state and hence different absorption coefficients such that the $\Delta T/T$ shows different magnitudes with increasing temperature. Also, when we change the pump-probe photon energy, as shown in Fig. 5, it is expected to observe different optical densities at a fixed temperature. Meanwhile, with localized band-gap renormalization, the induced band-gap shrinkage and potential-fluctuation reform may change the corresponding space-averaged density of state and hence the pump-probe behavior when the pump intensity is increased, as shown in Fig. 6.

When the corresponding density of state is high, a significant absorption leads to a strong band-filling effect, resulting in the high peaks around the zero pump-probe delay and the two-component decays. On the other hand, when the corresponding density of state is low, the band-filling effect is weak and hence two-photon absorption (TPA) and free-carrier absorption (FCA) become observable.²⁰ The sharp decreases or dips in some of the $\Delta T/T$ traces in Figs. 3, 4, and 6 are attributed to TPA. In these situations, the decays of the peaks right after the dips or the elongations of the dips are, at least partly, due to FCA. It is noted that TPA and FCA are expected to occur in any situation, either high or low density of state. However, they are prominent only when the band-filling effect is weak.

V. CONCLUSIONS

In summary, we have performed femtosecond degenerate pump-probe experiments on an InGaN thin film. The ob-

served temperature-, pump-photon-energy-, and pump-intensity-dependent variations of ultrafast carrier dynamics manifested the variation of space-averaged density of state along the energy level in the sample, in which potential fluctuations existed due to indium-composition fluctuations. The carrier dynamics was controlled by the shift of effective band gap and hence the behavior of band filling. The shift of effective band gap was determined by the combined effect of band-gap renormalization and phonon effect. TPA and FCA became observable when the density of state was low and hence the band-filling effect was weak. For the future work, the detailed variation of the space-averaged density of state in an InGaN thin film deserves further investigation.

ACKNOWLEDGMENTS

This research was supported by National Science Council, The Republic of China, under the Grant Nos. NSC 92-2210-M-002-006 and NSC 92-2215-E-002-010, and by US Air Force under the Contract No. AOARD-04-4026.

¹Y. S. Lin *et al.*, Appl. Phys. Lett. **77**, 2988 (2000).

²Y. S. Lin *et al.*, Appl. Phys. Lett. **80**, 2571 (2002).

³S. W. Feng *et al.*, Appl. Phys. Lett. **83**, 3906 (2003).

⁴Y. C. Cheng *et al.*, Appl. Phys. Lett. **84**, 2506 (2004).

⁵C. Wetzel, T. Takeuchi, H. Amano, and I. Akasaki, J. Appl. Phys. **85**, 3786 (1999).

⁶S. F. Chichibu *et al.*, Appl. Phys. Lett. **73**, 2006 (1998).

⁷E. Berkowicz *et al.*, Phys. Rev. B **61**, 10994 (2000).

⁸P. Perlin *et al.*, Appl. Phys. Lett. **73**, 2778 (1998).

⁹P. Riblet, H. Hirayama, A. Kinoshita, A. Hirata, T. Sugano, and Y. Aoyagi, Appl. Phys. Lett. **75**, 2241 (1999).

¹⁰I. Ho and G. B. Stringfellow, Appl. Phys. Lett. **69**, 2701 (1996).

¹¹S. Yu. Karpov, MRS Internet J. Nitride Semicond. Res. **3**, 16 (1998).

¹²Ü. Özgür and H. O. Everitt, Phys. Rev. B **67**, 155308 (2003).

¹³Y. Kawakami, Y. Narukawa, K. Omac, S. Fujita, and S. Nakamura, Appl. Phys. Lett. **77**, 2151 (2000).

¹⁴C. A. Parker, J. C. Roberts, S. M. Bedair, M. J. Reed, S. X. Liu, and N. A. El-Masry, Appl. Phys. Lett. **75**, 2776 (1999).

¹⁵S. W. Feng *et al.*, J. Appl. Phys. **95**, 5388 (2004).

¹⁶A. V. Kuznetsov and C. J. Stanton, Phys. Rev. B **51**, 7555 (1995).

¹⁷H. C. Wang, S. J. Lin, Y. C. Lu, Y. C. Cheng, C. C. Yang, and K. J. Ma, Appl. Phys. Lett. **85**, 1371 (2004).

¹⁸Ü. Özgür, C. W. Lee, and H. O. Everitt, Phys. Rev. Lett. **86**, 5604 (2001).

¹⁹Y. Kawakami, K. Omac, A. Kaneta, K. Okamoto, Y. Narukawa, T. Mukai, and S. Fujita, J. Phys.: Condens. Matter **13**, 6993 (2001).

²⁰M. Joschko, P. Langlois, E. R. Thoen, E. M. Koontz, and E. P. Ippen, Appl. Phys. Lett. **76**, 1383 (2000).



ELSEVIER

Available online at www.sciencedirect.com

SCIENCE @ DIRECT®

Journal of Crystal Growth ■■■■ ■■■■ ■■■■

JOURNAL OF CRYSTAL GROWTH

www.elsevier.com/locate/jcrysgro

Effects of silicon doping on the nanostructures of InGa_N/Ga_N quantum wells

Meng-Ku Chen^{a,b}, Yung-Chen Cheng^{a,b}, Jiun-Yang Chen^{a,b}, Cheng-Ming Wu^{a,b},
C.C. Yang^{a,b,*}, Kung-Jen Ma^c, Jer-Ren Yang^d, Andreas Rosenauer^e

^aGraduate Institute of Electro-Optical Engineering, Graduate Institute of Electronics Engineering, 1, Roosevelt Road, Section 4, Taipei, Taiwan, ROC

^bDepartment of Electro-Optical Engineering, National Taiwan University, 1, Roosevelt Road, Section 4, Taipei 106, Taiwan, ROC

^cDepartment of Mechanical Engineering, Chung Hua University, Hsinchu, Taiwan, ROC

^dDepartment of Material Science and Engineering, National Taiwan University, Taipei, Taiwan, ROC

^eLaboratorium für Elektronenmikroskopie, Universität Karlsruhe, 76128 Karlsruhe, Germany

Received 29 August 2004; accepted 7 February 2005

Communicated by G.B. Stringfellow

Abstract

We compare the results of strain state analysis (SSA) and photoluminescence (PL) of six InGa_N/Ga_N quantum well samples with un-doped, well-doped, and barrier-doped structures. Based on the SSA images, a strain relaxation model is proposed for describing the nanostructure differences between the three sets of sample of different doping conditions. In the barrier-doped samples, the hetero-structure-induced strains are fully relaxed such that spinodal decomposition is effectively induced. Therefore, strongly clustering nanostructures are observed. In the well-doped samples, strains are partially relaxed and the spinodal decomposition process can be slightly induced. Hence, weaker composition fluctuations are observed. Then, in the un-doped samples, the un-relaxed strains result in higher miscibility between InN and Ga_N, leading to the relatively more uniform composition distributions. Between the low- and high-indium samples, higher indium content leads to a stronger clustering behavior. The strain relaxations in the well-doped and barrier-doped samples result in their unclear S-shaped behaviors of PL spectral peaks. The enhanced carrier localization and reduced quantum-confined Stark effect in the barrier-doped samples are responsible for their significant increases of radiative efficiency.

© 2005 Published by Elsevier B.V.

PACS: ■; ■; ■

Keywords: ■; ■; ■

*Corresponding author. Institute of Electro-Optical Engineering, National Taiwan University, 1, Roosevelt Road, Section 4, Taipei 106, Taiwan, ROC. Tel.: +886 2 23657624; fax: +886 2 2365263.

E-mail address: ccy@cc.ee.ntu.edu.tw (C.C. Yang).

1. Introduction

It has been shown that different doping conditions, including different doping layers, in InGaN/GaN quantum well (QW) structures led to different optical characteristics. Such effects of silicon doping have been widely studied. Several models were proposed for interpreting the optical and material characteristics of InGaN/GaN QWs with silicon doping. The most commonly used model is the carrier screening effect of the strain-induced piezoelectric field and hence the reduction of the quantum-confined Stark effect (QCSE). This effect leads to the reduced Stokes shift [1–3], the decrease of radiative recombination lifetime [2–4,10], the blue shift of PL spectrum [3,5], and the enhancement of photon emission efficiency [1,3,6]. Also, material analyses have led to the conclusions of growth mode change [6], nanostructure alteration [7], formation of abrupt QW interfaces [2,8], strain relaxation [7,9], and higher potential uniformity in QWs [3]. Meanwhile, it has been shown that different barrier-doping concentrations in InGaN/GaN QW structures resulted in different optical characteristics [11]. These results are not necessarily mutually consistent, particularly in the material nanostructures of such silicon-doped QW samples.

In particular, due to the large lattice mismatch between InN and GaN, indium-rich clusters are usually formed in such a QW structure through spinodal decomposition and other effects [12–14]. In some situations, quantum-dot-like nanostructures can be observed [14–16]. With different silicon doping conditions, the clustering structures are expected different. Recently, the techniques of high-resolution transmission electron microscopy (HRTEM) have been widely used for understanding the properties of threading dislocations [17,18] and nano-structures in GaN and InGaN/GaN QW samples. In particular, the existence of indium-rich clusters in InGaN/GaN QW structures has been an interesting issue of discussion [19–22]. Although some researchers claimed that the observations of clusters were due to the artifacts [19,20], created through electron beam exposure during HRTEM measurements, the existence of clusters really relies on the conditions

of sample preparation. Under different conditions of crystal growth, clusters may or may not exist. Also, the cluster characteristics depend on those conditions.

In this paper, we use the strain-state analysis (SSA) method [23] to study the nanostructures of InGaN/GaN QWs of different doping conditions (un-doped, well-doped, and barrier-doped) and different average indium contents. It is found that the clustering phenomenon is the strongest in the barrier-doped samples and the weakest in the un-doped samples. Among the samples of different average indium contents, clustering behavior is relatively stronger in the high-indium samples. Based on the SSA results, the detailed nanostructures are analyzed and the relative indium contents can be confirmed. Besides, optical properties based on photoluminescence (PL) measurements are provided to show the consistent trends in the comparison of different doping conditions. This paper is organized as follows: in Section 2, the sample structures, growth conditions, and measurement procedures are reported. The SSA results of various samples are discussed in Section 3. Then, the optical characterization results are presented in Section 4. Certain discussions are given in Section 5. Finally, conclusions are drawn in Section 6.

2. Sample descriptions and experimental procedures

The six InGaN/GaN QW samples of different doping conditions and different average indium contents were prepared with MOCVD growth on sapphire (0001) substrate. They all consisted of five QW periods, with 2.5 nm in well width and 7.5 nm in barrier width, on top of an un-doped GaN buffer layer of 1.52 μm in thickness. The growth temperatures were 1100 and 800 $^{\circ}\text{C}$ for the GaN barriers and InGaN wells, respectively. The doping concentration of silicon was $5 \times 10^{18} \text{ cm}^{-3}$, either in barriers or wells. They are classified into two groups of low and high average indium contents. The low-indium set of samples has an estimated content of 15%. The high-indium set has indium content of 25% in estimation. In the low-indium set, the samples of un-doped, well-doped

and barrier-doped conditions were denoted with samples LU, LW, and LB, respectively. The counterparts of the high-indium set are assigned as samples HU, HW, and HB, respectively.

The HRTEM investigations (for SSA) were performed using a Philips Tecnai F30 field-emission electron microscope using an accelerating voltage of 300 kV and a probe-forming lens of $C_s = 1.2$ mm. All the high-resolution micrographs were taken with the two-electron-beam interference. The current density focused onto the samples was estimated to be lower than 16 A/cm^2 . With the two-beam interference data, we could conduct the SSA for composition distribution images [23]. In the HRTEM operation, to avoid the possible influence of electron illumination on the recorded results [19,20], the two-beam interference images were always taken within 5–10 s after the electron beam was focused onto the target spots. Our experiments showed that the processed SSA images were not significantly changed within 30 s of the illumination of focused electron beams. To obtain the SSA images, the $[0001]$ lattice size distributions were first calibrated from the lattice fringe images. Then, based on Vegard's law for the relation between the lattice size and indium composition, composition images could be obtained. These compositions were estimated based on the assumption of a specimen thickness larger than 50 nm. PL measurements were carried out with the 325 nm line of a 35 mW He–Cd laser. The samples were placed in a cryostat for temperature-dependent measurements ranging from 10 to 300 K.

3. Images of SSA

Figs. 1–6 show the typical SSA results of samples LU, LW, LB, HU, HW, and HB, respectively. In each figure, (a) shows the lattice fringe image of two-beam interference along the $[0001]$ direction and (b) shows the processed SSA image. One can see that the lattice fringe image cannot clearly describe the nanostructures of materials. The colors (gray levels) in the SSA image represent the estimated indium composition distributions. The relationship between the lattice

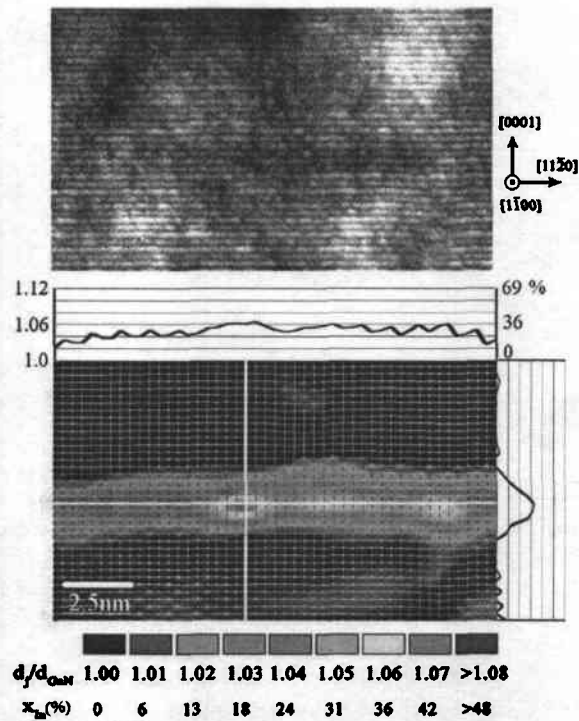


Fig. 1. Typical HRTEM lattice fringe image (a) and the SSA image (b) after software process of samples LU.

parameter ratio d_j/d_{GaNN} (d_{GaNN} and d_j for the lattice sizes of GaN and InGaN, respectively) and the indium composition x_{in} (%) is shown in the legend at the bottom of the figure. It is noted that their relationship is not linear, particularly when the indium composition is high. In each SSA image, line scan profiles of indium composition along the indicated white lines are plotted. The scales for the profiles in the two dimensions are the same. In each SSA image, a QW surrounded by the two barriers are illustrated.

Fig. 1(b) shows the SSA image of sample LU. One can see that the QW layer (green region) is quite uniform. The indium clusters (reddish or dark regions) within the QW layer are quite small and shallow. The GaN barriers (deep blue or bright regions) are clear. It means that indium is well confined within the well. From the horizontal line-scan profile, one can observe quite a weak fluctuation in indium composition along the well layer. The fluctuation contrast (the difference

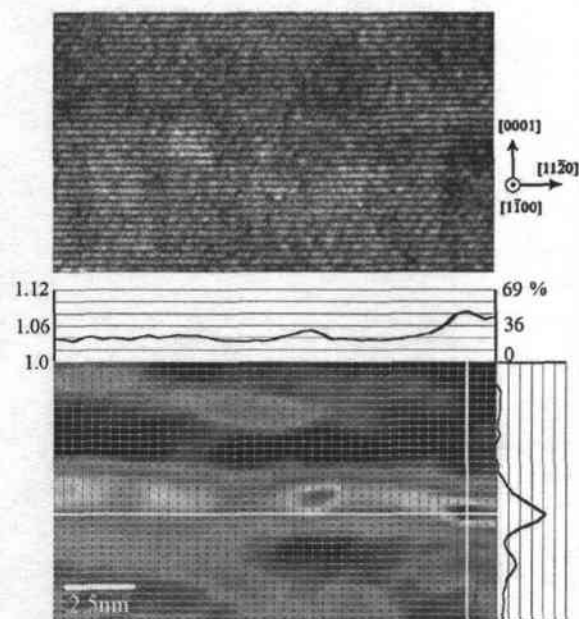


Fig. 2. Typical HRTEM lattice fringe image (a) and the SSA image (b) after software process of samples LW.

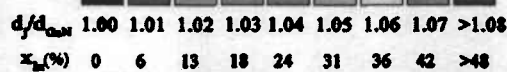
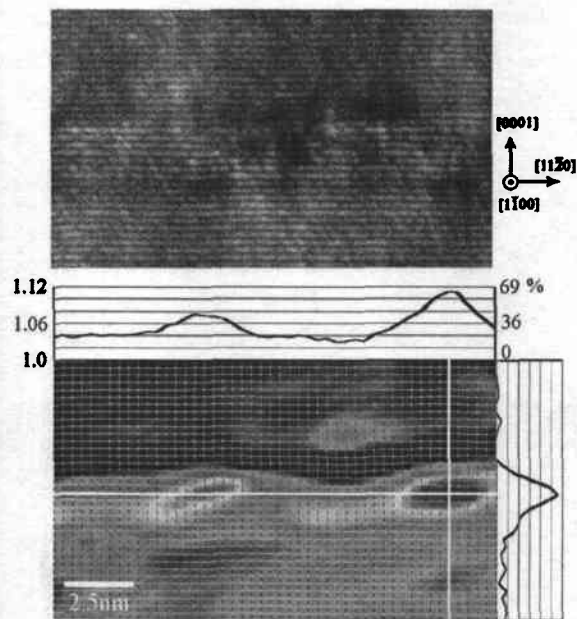


Fig. 3. Typical HRTEM lattice fringe image (a) and the SSA image (b) after software process of samples LB.

between the maximum and the minimum in the scan range) is in the range of 0.03–0.04 (18–24%) along the QW layer. In Fig. 2(b) for sample LW, we can observe that more indium clusters are formed in the QW layer. Also, more indium atoms diffuse from the well into barriers. Here, the fluctuations of the line-scan profiles are relatively stronger in comparing with those of sample LU. The fluctuation contrast is now in the range of 0.04–0.05 (22–28%). In Fig. 3(b) for sample LB, we can see two clear indium-rich clusters in the QW (two large red spots). From the line-scan profiles, one can see that the indium composition fluctuation in sample LB is much stronger than those of the other two samples. The fluctuation contrast is now around 0.08 (44%).

As shown in Fig. 4(b) for sample HU, although the QW interface is blurred, indium is basically confined within the well. Here, within the well a red spot of indium aggregation can be observed. Similar to sample LU, one can also observe a

relatively weaker fluctuation in indium composition along the well layer in the line-scan profile. The fluctuation contrast is about 0.04 (22%) along the QW layer. In Fig. 5(b) for the SSA image of sample HW, the QW is not as well shaped as sample HU. The indium composition fluctuations in both directions are relatively stronger in comparing with sample HU. In particular, more indium-aggregated clusters can be observed within the well layer. The fluctuation contrast is also around 0.04 (22%) along the QW layer. As shown in Fig. 6(b), the SSA image of sample HB shows quite a different nanostructure from the other five samples. Here, the QW layer becomes unclear. Instead, a distribution of clusters of different sizes and shapes exists. The indium composition fluctuation is much stronger than those of samples HU and HW. The contrast is now around 0.08 (44%) along the QW layer.

A question has been raised about the possible influence of electron beam exposure on the

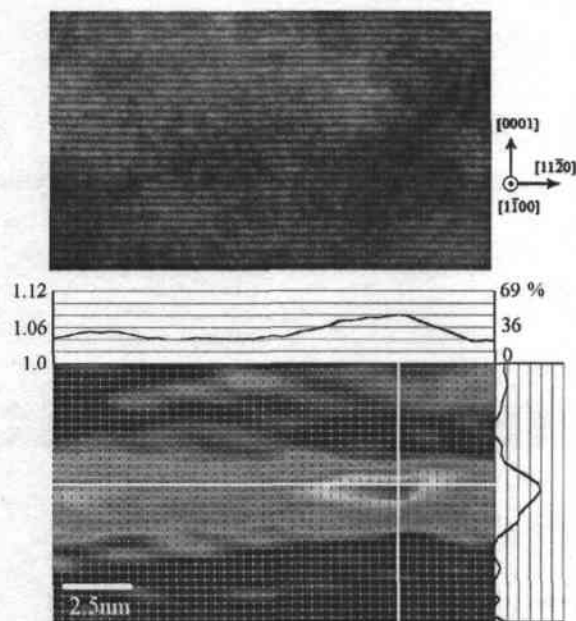


Fig. 4. Typical HRTEM lattice fringe image (a) and the SSA image (b) after software process of samples HU.

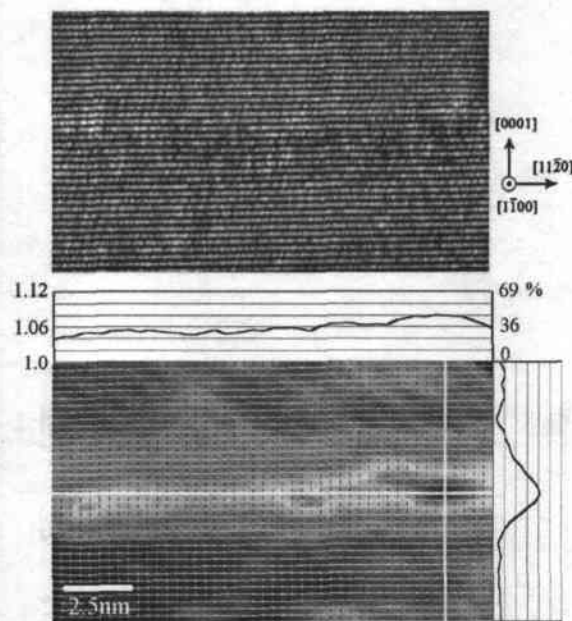


Fig. 5. Typical HRTEM lattice fringe image (a) and the SSA image (b) after software process of samples HW.

material nanostructures during the measurement of transmission electron microscopy [19,20]. We have tested such a possibility by varying the electron exposure time. The SSA images of sample LB shown in Fig. 7(a) and (b) were obtained under electron beam exposure for less than 10 s and about 2 min, respectively. Fig. 7(a) is different from Fig. 3(b) because they were obtained at different locations of sample LB. Between Fig. 7(a) and (b), one can see that although the details are slightly changed, the basic structures are the same. In other words, with up to 2-min exposure, we can still obtain the required information about the nanostructures of the samples. Normally, when we operated the HRTEM system, it took less than 10 s after the electron beam was focused onto a target spot to obtain an image. In our research, we have done our best to reduce the electron beam effect. Hence, the SSA images in this research can truly represent the sample nanostructures.

In Figs. 8 and 9, we show the average line-scan profiles in the [0001] direction, averaged over the image range along the [11-20] direction, plotted as functions of distance for the low- and high-indium samples, respectively. Two to three SSA images like Figs. 1–6 at different locations in each sample were used for taking the average. One can see that generally the well widths of the high-indium samples are larger than those of the low-indium ones. One can also observe that the interfaces between the well and barriers of the low-indium samples are generally sharper than those of the high-indium ones. Meanwhile, generally the indium concentrations at the peaks of the high-indium samples are higher than those of the low-indium ones. In addition, in the low-indium samples, more indium atoms diffuse from the well into the lower barrier. Indium out-diffusion in the high-indium samples is more symmetric.

The average indium content of each sample can be calibrated by integrating the average line-scan

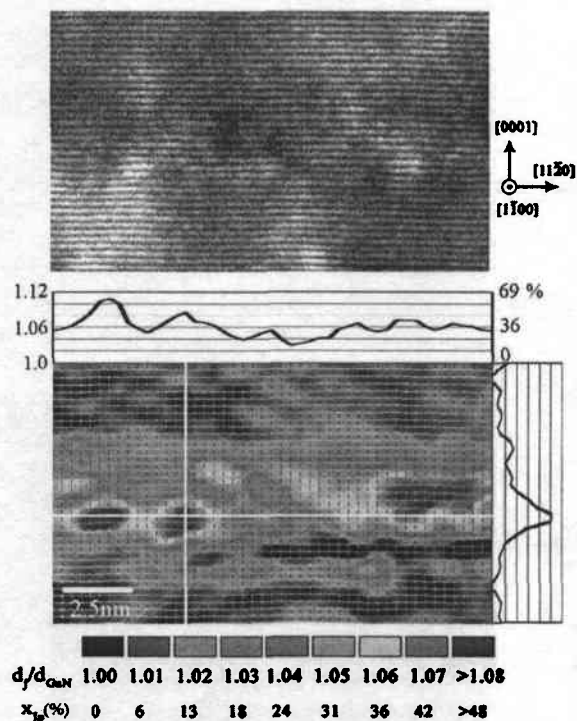


Fig. 6. Typical HRTEM lattice fringe image (a) and the SSA image (b) after software process of samples HB.

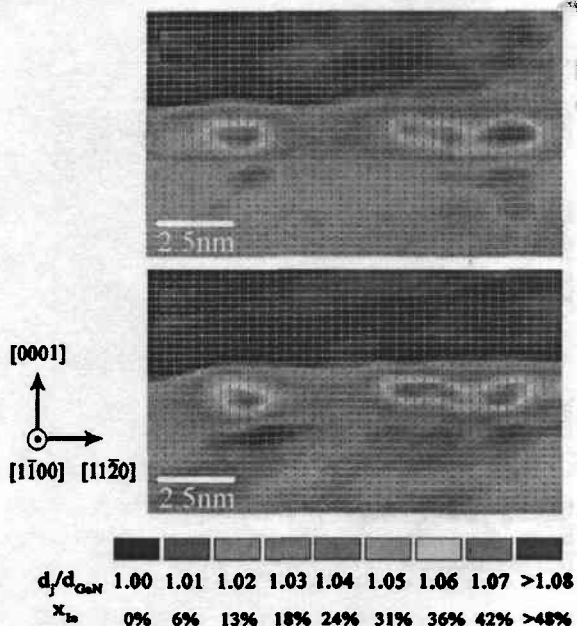


Fig. 7. SSA images of sample LB under different electron-beam exposure times: (a) <10 s and (b) 120 s.

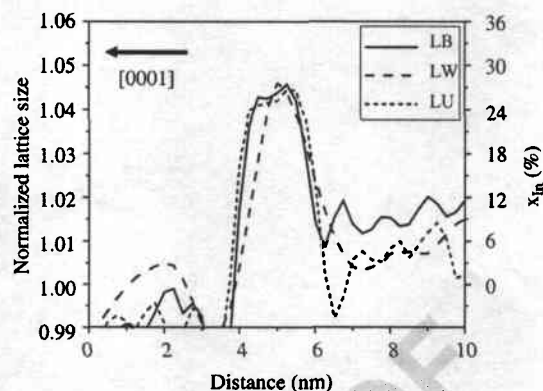


Fig. 8. Average indium composition profiles along the crystal growth direction for samples LU, LW, and LB.

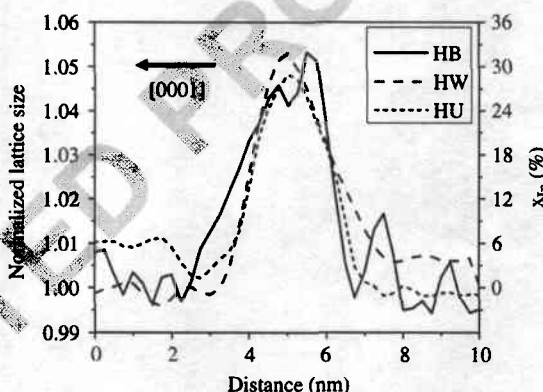


Fig. 9. Average indium composition profiles along the crystal growth direction for samples HU, HW, and HB.

results in Figs. 8 or 9 over the whole range and then dividing the integrated result by the designated QW width (2.5 nm). The whole-range integration implies the coverage of the indium atoms, which diffuse from the well into barriers. Such results of average indium content become more accurate if more SSA images like Figs. 1–6 are used for average. Although the current results cannot be very accurate, they can still be used for a general comparison. The calibrated average indium contents of samples LU, LW, and LB are 14.3%, 17.1%, and 19.2%, respectively. Those of samples HU, HW, and HB are 25.6%, 26.7%, and 26.9%, respectively. These results are generally consistent with the designated indium contents of 15% and 25% for the low- and high-indium

samples, respectively. The generally higher indium contents from calibration for the barrier- and well-doped samples can be attributed to the stronger indium diffusion into barriers in these two kinds of sample. With more indium atoms in the barriers, the calibration for indium composition in processing the SSA images can be overestimated. However, the possibility of really higher average indium content in the doped samples cannot be ruled out. With different strain conditions (due to different doping conditions), the incorporation efficiency of indium atom can be different even the flow rate is the same during growth.

4. Optical characterization results

To understand the corresponding optical properties of these samples, basic optical characterizations were performed. Fig. 10 shows the PL spectral peak positions as functions of temperature

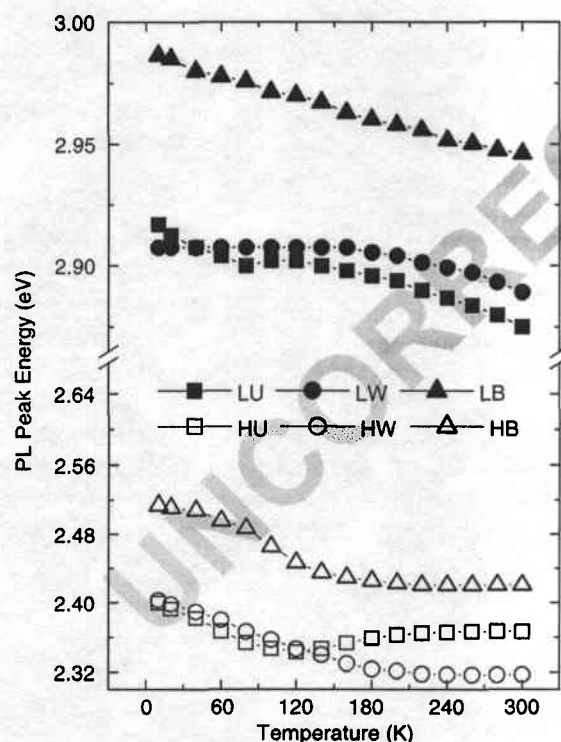


Fig. 10. PL spectral peak variations with temperature of the six samples.

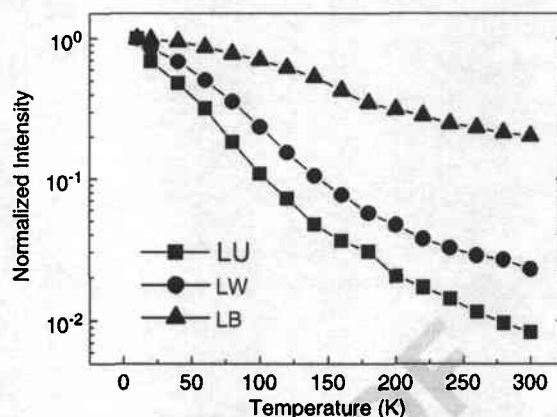


Fig. 11. Integrated PL intensity variations with temperature of samples LU, LW, and LB.

for all the six samples with the filled and empty symbols for the low- and high-indium samples, respectively. Clear S-shaped variations can be seen in the curves for samples LU and HU. On the contrary, the S-shaped behaviors are unclear in the well- and barrier-doped samples. The PL peak positions of the un-doped and well-doped samples in either group of sample are quite close, particularly in the low-temperature range. The significant blue shifts of the PL peaks of samples LB and HB, with respect to those of the un-doped and well-doped samples show a clear feature of barrier doping.

Fig. 11 shows the integrated PL intensities as functions of temperature of samples LU, LW, and LB. Fig. 12 shows the counterparts of samples HU, HW, and HB. The thermal quenching behavior in integrated luminescence intensity represents the radiative efficiency. From Figs. 11 and 12, one can see that the barrier-doped samples always have the highest radiative efficiency, followed by the well-doped samples and then the un-doped samples. Hence, in our samples, silicon doping, particularly doping in barriers, can lead to a higher efficiency of spontaneous emission.

5. Discussions

The SSA images show that barrier doping results in stronger indium clustering. This result

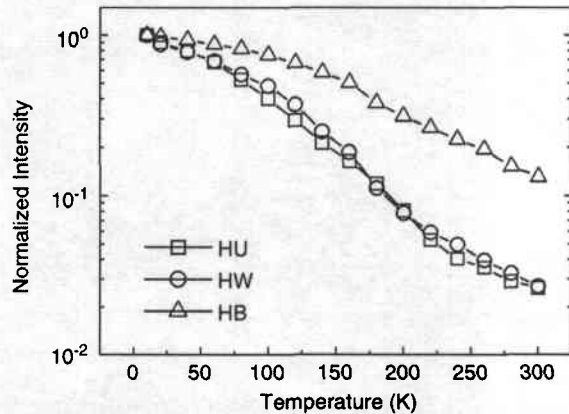


Fig. 12. Integrated PL intensity variations with temperature of samples HU, HW, and HB.

may be caused by the significant relaxation of hetero-structure-induced strain (the strain in QW due to the lattice mismatch between wells and barriers) in the barrier-doped samples, particularly in sample HB, through certain mechanisms. In sample HB, with the growth temperature at 800 °C and nominal indium content about 25%, the sample condition falls into the regime of spinodal decomposition (the unstable regime) in the T - x phase diagram of ternary $\text{In}_x\text{Ga}_{1-x}\text{N}$ compounds for relaxed and strained layers with the interface orientation perpendicular to the hexagonal axis of the crystal [12,24]. In this regime, spinodal decomposition and phase separation can be initiated by a small local compositional fluctuation. Hence, strongly clustering behaviors can be observed in sample HB. The mechanisms for relaxing the hetero-structure-induced strain can be the generation of local dislocations, which is caused by the enhanced lattice mismatch between a well and the surrounding barriers because of the substitutions of a high-concentration of larger gallium atoms (atomic weight as 31) by smaller silicon atoms (atomic weight as 14) in the barriers. The HRTEM images in the similar samples of our and other's previous research have shown the existence of local dislocations in an InGaN/GaN QW sample of a high nominal indium content [25,26]. The other mechanism for strain relaxation in the barrier-doped sample is the existence of plenty carriers in the barriers and wells (carriers

flow into wells) due to the heavy silicon doping in the barriers. The carriers screen the piezoelectric fields and affect the strain energy distributions. However, it is believed that the major mechanism for strain relaxation is the formation of local dislocations. The discussions described above fit well the conditions of sample HB. In sample LB, because the nominal indium content is lower (about 15%), the hetero-structure-induced strain is not as strong as that in sample HB. Therefore, the condition may fall into a region between the unstable and metastable regimes in the T - x phase diagram. In this situation, spinodal decomposition and phase separation processes can still be induced. However, these processes in the metastable regime take a longer time than that in the unstable regime, leading to a relatively weaker clustering behavior.

In the well-doped samples, because of the substitutions of larger gallium or indium atoms by smaller silicon atoms (lattice mismatch reduced) and the effect of carrier screening, the hetero-structure-induced strain has been partly relaxed such that the conditions may belong to the meta-stable regime in the T - x phase diagram. Hence, certain clusters were generated although the clustering behaviors are not as strong as those in the barrier-doped samples. In the un-doped samples, the strong hetero-structure-induced strains are preserved such that the conditions are essentially located in the stable regime. In this situation, the solubility of InN in GaN is higher such that the clustering behaviors are the weakest among the three kinds of sample. It is noted that with a higher nominal indium content, the condition in the phase diagram can be closer to the meta-stable or even spinodal decomposition regime and hence the clustering behavior can be stronger.

From the SSA results above, we can build a model for potential variation along a QW layer. In the situations of samples HU and LU, potential fluctuations are weak. A potential minimum is surrounded by secondary minima of shallow barriers in between. In the cases of samples HW and LW, potential variations are relatively stronger. In this situation, a potential minimum is also surrounded by secondary minima. However, the

barriers between the minima are now relatively higher such that certain energy is required for carrier transport between the minima. Then, for samples HB and LB, sharp minima with few secondary dips are assumed. Therefore, carriers can relax down to the absolute potential minima without a cascading process through the secondary minima. The difference between the well-doped and un-doped samples is that more energy is required for overcoming the barriers in samples LW and HW.

The relative larger PL photon energies in the barrier-doped samples can be due to the reduction of piezoelectric fields that originates from strain relaxation and carrier screening. Also, it can be due to the increase of quantum confinement, which results from the formation of nano-scale clusters. In the well-doped samples, more carriers in the well layers should result in significant increases of PL photon energies due to strong carrier screening. However, the PL photon energies of the well-doped samples are quite close to those of the un-doped samples. Such a result can be attributed to the ineffective carrier screening effect. It can also be interpreted as the result of the counteraction between band gap renormalization (red-shift trend) and piezoelectric field reduction (blue-shift trend). As shown in Fig. 10, the temperature-dependent PL spectral peak energies reveal clear S-shaped behaviors in samples LU and HU. Such an S-shaped behavior is usually attributed to carrier localization [27,28] and/or QCSE [29,30]. Because the S-shaped behavior is unclear in either well-doped or barrier-doped samples, whose strains are supposed to be partially or fully relaxed, the major mechanism for the S-shaped behavior in our samples must be the strain distribution or QCSE. Without significant relaxation of strains in the un-doped samples, the S-shaped behaviors are quite prominent. The significant enhancement of radiative recombination efficiency in the barrier-doped samples can be attributed to the strong carrier localization (localized from non-radiative recombination centers) and the reduced QCSE (improved wave function overlap between electron and hole).

6. Conclusions

In summary, we have compared the results of SSA and PL of six InGaN/GaN QW samples with un-doped, well-doped, and barrier-doped structures. Based on the SSA images, a strain relaxation model was built for describing the nanostructure differences between the three sets of sample of different doping conditions. In the barrier-doped samples, the hetero-structure-induced strains were fully relaxed such that spinodal decomposition was effectively induced. Therefore, strongly clustering nanostructures were observed. In the well-doped samples, strains were partially relaxed and the spinodal decomposition process could be slightly induced. Hence, weaker composition fluctuations were observed. Then, in the un-doped samples, the un-relaxed strains resulted in higher miscibility between InN and GaN, leading to the relatively more uniform composition distributions. Between the low- and high-indium samples, higher indium content led to a stronger clustering behavior. The strain relaxations in the well-doped and barrier-doped samples resulted in their unclear S-shaped behaviors of PL spectral peaks. The enhanced carrier localization and reduced QCSE in the barrier-doped samples were responsible for their significant increases of radiative efficiency.

Acknowledgements

This research was supported by National Science Council, The Republic of China, under the Grant of NSC 92-2210-M-002-006 and NSC 92-2215-E-002-010, and by US Air Force under the Contract AOARD-04-4026.

References

- [1] S. Chichibu, D.A. Cohen, M.P. Mack, A.C. Abare, P. Kozodoy, M. Minsky, S. Fleischer, S. Keller, J.E. Bowers, U.K. Mishra, L.A. Coldren, D.R. Clarke, S.P. DenBaars, *Appl. Phys. Lett.* 73 (1998) 496.
- [2] Y.H. Cho, J.J. Song, S. Keller, M.S. Minsky, E. Hu, U.K. Mishra, S.P. DenBaars, *Appl. Phys. Lett.* 73 (1998) 1128.
- [3] M.S. Minsky, S. Chichibu, S.B. Fleischer, A.C. Abare, J.E. Bowers, E.L. Hu, S. Keller, U.K. Mishra, S.P. DenBaars, *Jpn. J. Appl. Phys.* 37 (1998) L1362.

- [4] M.Y. Ryu, Y.J. Yu, E.J. Shin, P.W. Yu, J.I. Lee, S.K. Yu, E.S. Oh, O.H. Nam, C.S. Sone, Y.J. Park, T.I. Kim, Solid State Commun. 116 (2000) 675.
- [5] J. Dalfors, J.P. Bergman, P.O. Holtz, B.E. Sernelius, B. Monemar, H. Amano, I. Akasaki, Appl. Phys. Lett. 74 (1999) 3299.
- [6] K. Uchida, T. Tang, S. Goto, T. Mishima, A. Niwa, J. Gotoh, Appl. Phys. Lett. 74 (1999) 1153.
- [7] Y.C. Cheng, Cheng-Hua Tseng, Chen Hsu, Kung-Jen Ma, Shih-Wei Feng, En-Chiang Lin, C.C. Yang, Jen-Inn Chyi, J. Electron. Mater. 32 (2003) 375.
- [8] Y.H. Cho, F. Fedler, R.J. Hauenstein, G.H. Park, J.J. Song, S. Keller, U.K. Mishra, S.P. DenBaars, J. Appl. Phys. 85 (1999) 3006.
- [9] S. Ruvimov, Z. Liliental-Weber, T. Suski, J.W. Ager III, J. Washburn, J. Krueger, C. Kieselowski, E.R. Weber, H. Amano, I. Akasaki, Appl. Phys. Lett. 69 (1996) 990.
- [10] C.K. Choi, Y.H. Kwon, B.D. Little, G.H. Gainer, J.J. Song, Y.C. Chang, S. Keller, U.K. Mishra, S.P. DenBaars, Phys. Rev. B 64 (2001) 245339-1.
- [11] M.Y. Ryu, P.W. Yu, E. Oh, C. Sone, O. Nam, Y. Park, Solid State Commun. 118 (2001) 547.
- [12] I. Ho, G.B. Stringfellow, Appl. Phys. Lett. 69 (1996) 2701.
- [13] Y.S. Lin, K.J. Ma, C. Hsu, S.W. Feng, Y.C. Cheng, C.C. Liao, C.C. Yang, C.C. Chu, C.M. Lee, J.I. Chyi, Appl. Phys. Lett. 77 (2000) 2988.
- [14] Y.S. Lin, K.J. Ma, C. Hsu, Y.Y. Chung, C.W. Liu, S.W. Feng, Y.C. Cheng, M.H. Mao, C.C. Yang, H.W. Chuang, C.T. Kuo, J.S. Tsang, T.E. Weirich, Appl. Phys. Lett. 80 (2002) 2571.
- [15] Y.S. Lin, K.J. Ma, C.C. Yang, T.E. Weirich, J. Crystal Growth 242 (2002) 35.
- [16] R. Seguin, S. Rodt, A. Strittmatter, L. Reissmann, T. Bartel, A. Hoffmann, D. Bimberg, E. Hahn, D. Gerthsen, Appl. Phys. Lett. 84 (2004) 4023.
- [17] J. Bai, T. Wang, Y. Izumi, S. Sakai, J. Crystal Growth 223 (2001) 61.
- [18] H.K. Cho, J.Y. Lee, C.S. Kim, G.M. Yang, N. Sharma, C. Humphreys, J. Crystal Growth 231 (2001) 466.
- [19] T.M. Smeeton, M.J. Kappers, J.S. Barnard, M.E. Vickers, C.J. Humphreys, Appl. Phys. Lett. 83 (2003) 5419.
- [20] J.P. O'Neill, I.M. Ross, A.G. Cullis, T. Wang, P.J. Parbrook, Appl. Phys. Lett. 83 (2003) 1965.
- [21] Y.C. Cheng, E.C. Lin, C.M. Wu, C.C. Yang, J.R. Yang, A. Rosenauer, K.J. Ma, S.C. Shi, L.C. Chen, C.C. Pan, J.I. Chyi, Appl. Phys. Lett. 84 (2004) 2506.
- [22] Y.C. Cheng, C.M. Wu, M.K. Chen, C.C. Yang, Z.C. Feng, G.A. Li, J.R. Yang, A. Rosenauer, K.J. Ma, Appl. Phys. Lett. 84 (2004) 5422.
- [23] D. Gerthsen, B. Neubauer, A. Rosenauer, T. Stephan, H. Kalt, O. Schon, M. Heuken, Appl. Phys. Lett. 69 (1996) 2701.
- [24] S.Yu. Karpov, J. Nitride Semicond. Res. 3 (1998) 16.
- [25] Y.S. Lin, C.C. Yan, C. Hsu, K.J. Ma, Y.Y. Chung, S.W. Feng, Y.C. Cheng, E.C. Lin, C.C. Yang, C.T. Kuo, J.S. Tsang, J. Crystal Growth 252 (2003) 107.
- [26] H.K. Cho, J.Y. Lee, J.Y. Leam, Appl. Surf. Sci. 221 (2004) 288.
- [27] Y.H. Cho, G.H. Gainer, A.J. Fischer, J.J. Song, S. Keller, U.K. Mishra, S.P. DenBaars, Appl. Phys. Lett. 73 (1998) 1370.
- [28] T. Matsuoka, H. Okamoto, M. Nakao, H. Harima, E. Kurimoto, Appl. Phys. Lett. 81 (2002) 1246.
- [29] S.F. Chichibu, A.C. Abare, M.S. Minsky, S. Keller, S.B. Fleischer, J.E. Bowers, E. Hu, U.K. Mishra, L.A. Coldren, S.P. DenBaars, T. Sota, Appl. Phys. Lett. 73 (1998) 2006.
- [30] E. Berkowicz, D. Gershoni, G. Bahir, E. Lakin, D. Shilo, E. Zolotoyabko, A.C. Abare, S.P. DenBaars, L.A. Coldren, Phys. Rev. B 61 (2000) 10994.